cmgh
CELLULAR AND MOLECULAR GASTROENTEROLOGY AND HEPATOLOGY

ORIGINAL RESEARCH

Post-COVID-19 Effects on Chronic Gastritis and Gastric Cellular and Molecular Characteristics in Male Mice

Haengdueng Jeong,[1,2] Sung-Hee Kim,[1] Jiseon Kim,[1] Donghun Jeon,[1] Chanyang Uhm,[1] Heeju Oh,[1] Kyungrae Cho,[1] In Ho Park,[1,3] Jooyeon Oh,[4] Jeong Jin Kim,[1] Sang-Ho Jeong,[5] Ji-Ho Park,[5] Jun Won Park,[8] Jun-Won Yun,[9] Jun-Young Seo,[1] Jeon-Soo Shin,[1,3,4] James R. Goldenring,[2] Je Kyung Seong,[6,7,10,11] and Ki Taek Nam[1]

[1]Department of Biomedical Sciences, Brain Korea 21 PLUS Project for Medical Science, Yonsei University College of Medicine, Seoul, South Korea; [2]Epithelial Biology Center and Department of Surgery, Vanderbilt University School of Medicine, Nashville, Tennessee; [3]Institute of Immunology and Immunological Diseases, Yonsei University College of Medicine, Seoul, South Korea; [4]Department of Microbiology, Yonsei University College of Medicine, Seoul, South Korea; [5]Department of Surgery, Gyongsang National University Hospital, Jinju, Korea; [6]Korea Mouse Phenotyping Center, Seoul National University, Seoul, South Korea; [7]Laboratory of Developmental Biology and Genomics, Research Institute for Veterinary Science, Brain Korea 21 PLUS Program for Creative Veterinary Science Research, College of Veterinary Medicine, Seoul National University, Seoul, South Korea; [8]Laboratory Animal Medicine, College of Veterinary Medicine, Seoul National University, Seoul, South Korea; [9]Laboratory of Veterinary Toxicology, College of Veterinary Medicine, Seoul National University, Seoul, South Korea; [10]BIO-MAX Institute, Seoul National University, Seoul, South Korea; and [11]Interdisciplinary Program for Bioinformatics, Seoul National University, Seoul, South Korea

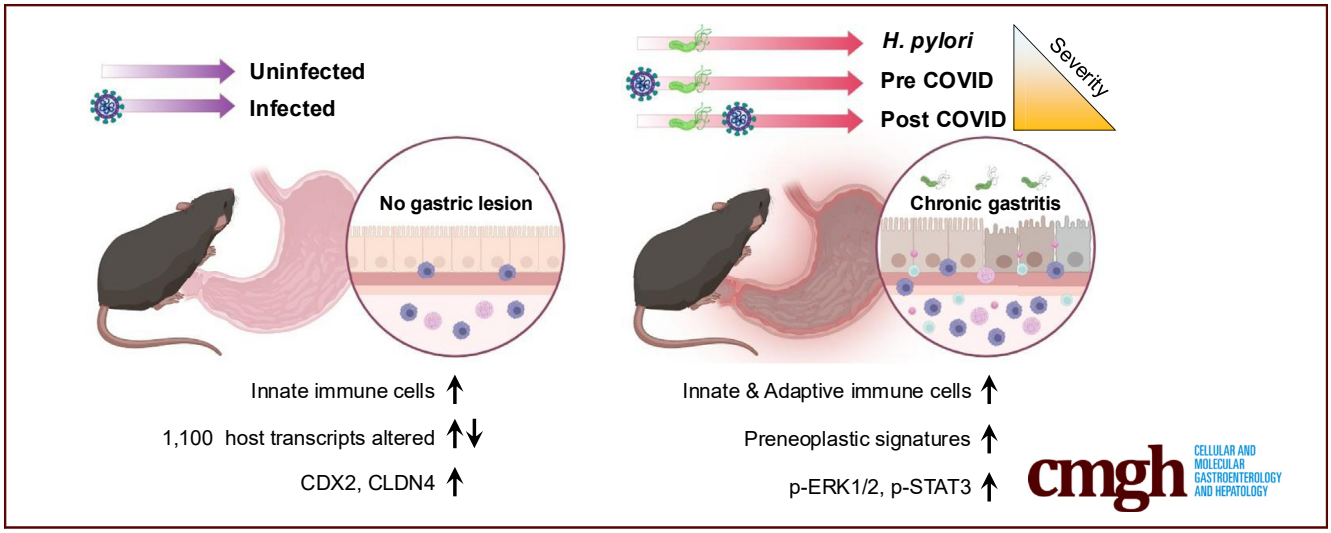

SUMMARY

The increase in disease severity was particularly prominent in mice that developed COVID-19 after *H pylori*. Overall, This study shed light on the negative effect of severe acute respiratory syndrome coronavirus 2 on gastric disease.

BACKGROUNDS & AIMS: Since the Omicron variant emerged as a major severe acute respiratory syndrome coronavirus 2 (SARS-CoV-2) variant, COVID-19-associated mortality has decreased remarkably. Nevertheless, patients with a history of SARS-CoV-2 infection have been suffering from an aftereffect commonly known as 'long COVID,' affecting diverse organs. However, the effect of SARS-CoV-2 on gastric cells and disease progression was not previously known. We aimed to investigate whether SARS-CoV-2 infection affects stomach cells and if post-COVID-19 conditions can lead to severe gastric disease.

METHODS: Stomach specimens obtained from male K18-hACE2 mice 7 days after SARS-CoV-2 infection were subjected to a transcriptomic analysis for molecular profiling. To investigate the putative role of SARS-CoV-2 in gastric carcinogenesis, K18-hACE2 mice affected by nonlethal COVID-19 were also inoculated with *Helicobacter pylori* SS1.

RESULTS: Despite the lack of viral dissemination and pathologic traits in the stomach, SARS-CoV-2 infection caused dramatic changes to the molecular profile and some immune subsets in this organ. Notably, the gene sets related to metaplasia and gastric cancer were significantly enriched after viral infection. As a result, chronic inflammatory

responses and preneoplastic transitions were promoted in these mice.

CONCLUSION: SARS-CoV-2 infection indirectly leads to profound and post-acute COVID-19 alterations in the stomach at the cellular and molecular levels, resulting in adverse outcomes following co-infection with SARS-CoV-2 and *H pylori*. Our results show that 2 prevalent pathogens of humans elicit a negative synergistic effect and provide evidence of the risk of severe chronic gastritis in the post-COVID-19 era. *(Cell Mol Gastroenterol Hepatol 2025;19:101511; https://doi.org/10.1016/j.jcmgh.2025.101511)*

Keywords: Chronic Gastritis; *Helicobacter pylori*; Post-acute COVID-19 Syndrome; Virus and Diseases.

In March 2020, COVID-19 was declared a Public Health Emergency by the World Health Organization, and this novel virus was responsible for more than 3 million global deaths in 2020. Severe acute respiratory syndrome coronavirus 2 (SARS-CoV-2) is the etiological agent of COVID-19 and enters host cells via the respiratory tract, promoting the formation of severe pulmonary lesions, acute immune responses, and systemic diseases.[1,2] Because in vitro assays cannot simulate human pathophysiology, proper animal models are required to understand COVID-19. Some preclinical models, such as K18-promoter-driven human ACE2-expressing (K18-hACE) mice, Syrian golden hamsters, ferrets, and non-human primates, can be used to mimic COVID-19 clinical signs and morbidities in patients.[3,4]

Owing to the emergence of less severe variants and widespread vaccination, COVID-19-associated mortality has been decreasing.[5] Nevertheless, the threat of COVID-19 remains because the virus causes diverse symptoms in multiple organs.[3,6,7] Recently, many studies have focused on the subsequent effects of SARS-CoV-2 infection, referred to it as 'long COVID' or the 'post-COVID condition.' Indeed, patients infected with SARS-CoV-2 suffer from ongoing health problems with systemic manifestations in the cardiovascular, reproductive, neurological, and gastrointestinal (GI) tracts.[8,9] Moreover, this novel virus appears to exert a synergistic effect with pre-existing inflammatory diseases in humans, eliciting adverse effects after COVID-19.[10–12]

Gastric cancer is the fifth most common cancer worldwide, and intestinal-type adenocarcinoma sequentially progresses through multiple stages, including oxyntic atrophy (parietal cell loss), preneoplastic metaplasia (spasmolytic polypeptide-expressing metaplasia and intestinal metaplasia), dysplasia, and eventually cancer.[13–15] Parietal cell loss is a primary event during gastric carcinogenesis, causing chief cell transdifferentiation and subsequent profound alterations in cellular and molecular profiles.[16–18] Notably, some prevalent markers in patients with cancer cause the development of metaplastic and neoplastic cells.[19–21] Although many gastric cancer risk factors have been suggested, *Helicobacter pylori* predominantly affects gastric cancer risk by mediating chronic inflammation, with more than 50% of the global population already infected with this pathogen. Diverse immune subsets are activated in response to *H pylori* infection, and the relevant inflammatory responses putatively accelerate gastric disease progression.[22–25]

The GI tract is also a SARS-CoV-2-target site and is associated with the subsequent post-acute effects of COVID-19, which causes multiple GI disorders.[8,9,26] Intestinal epithelial cells express hACE2 and can be infected by SARS-CoV-2.[27,28] In addition, this novel virus can survive in intestinal cells for several months and induce transcriptome alterations.[29,30] However, whether SARS-CoV-2 infects gastric cells or affects disease progression remains unclear. Most importantly, the association between novel coronaviruses and *H pylori*, among the most prevalent pathogens globally, is not understood. Further, few clinical studies support the negative synergistic effect of *H pylori* and Epstein-Barr virus (EBV), which is related to gastric cancer.[31,32] This study aimed to determine the effect of COVID-19 on stomach cellular and molecular profiles and the progression of *H pylori*-induced gastric disease. To explore the underlying mechanisms, we utilized K18-hACE2 mice infected with SARS-CoV-2 and found that SARS-CoV-2 affects *Helicobacter*-induced gastritis through dynamic changes in transcriptomics and immune cells.

Results

SARS-CoV-2 Does Not Disseminate to the Stomach but Affects the Immune Cell Composition

In total, 10^6 plaque-forming units of SARS-CoV-2 were inhaled into K18-hACE2 mice, which were euthanized 2, 5, 7, and 14 days and 4 weeks after viral infection (Figure 1*A*). In line with our previous result,[3] SARS-CoV-2 immediately spread throughout the lung parenchyma after infection, concomitant with acute respiratory diseases, for 7 days (Figure 1*A and B*). Although SARS-CoV-2 was eliminated from the lungs 14 days and 4 weeks after viral infection, fibrosis and mild inflammatory foci remained (Figure 1*B*). In contrast, SARS-CoV-2 infection did not induce disease progression in the stomach or disrupt glandular structures (Figure 1*C*). Even at 7 days post-infection (dpi), when the viral concentration and acute inflammation peaked in the lungs, pathologic signs and SARS-CoV-2 were devoid in the stomach (Figure 1*B and C*).

Abbreviations used in this paper: **ABL3, Animal Biosafety Level 3; ANOVA, analysis of variance; CFU, colony-forming unit; DEGs, differentially expressed genes; dpi, days post-infection; EBV, Epstein-Barr virus; FBS, fetal bovine serum; GI, gastrointestinal; GSEA, Gene set enrichment analysis; H&E, hematoxylin and eosin; HRP, horseradish peroxidase; IHC, immunohistochemistry; K18-hACE, K18-promoter-driven human ACE2-expressing; PBS, phosphate-buffered saline; RT, room temperature; RT-qPCR, reverse transcription-quantitative polymerase chain reaction; SARS-CoV-2, severe acute respiratory syndrome coronavirus 2; SEM, standard error of the mean; T4SS, Type 4 secretion system.**

Most current article

2352-345X
https://doi.org/10.1016/j.jcmgh.2025.101511

In contrast to severe COVID-19, which leads to death, mild clinical signs and a convalescent phase have been identified in mice that inhaled SARS-CoV-2. A slight reduction in body weight was observed in the K18-hACE2 mice at 7 dpi (Figure 1*D*). In addition, mild lymphopenia and neutrophilia were recapitulated at 7 dpi (Figure 1*E*).

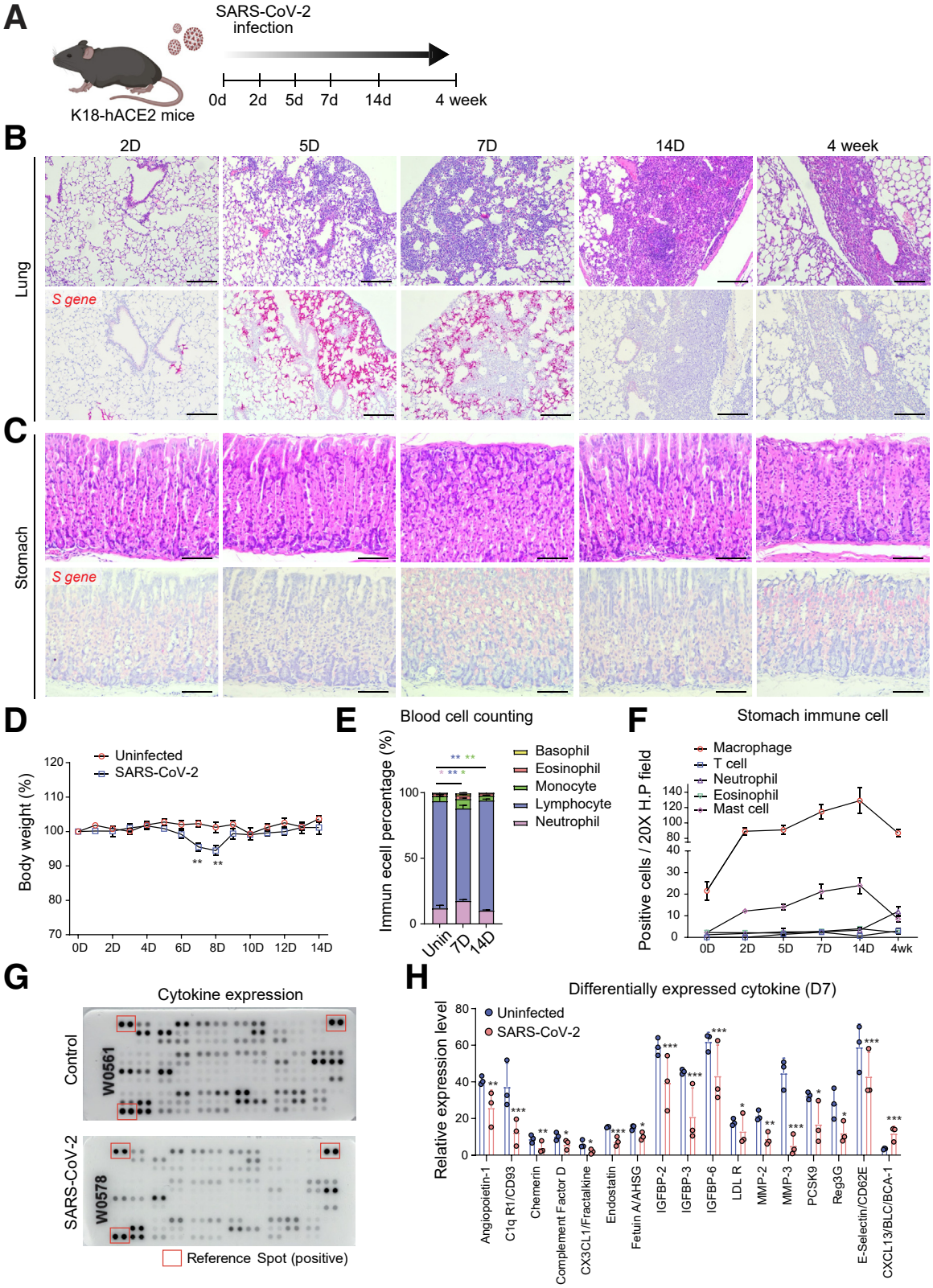

These clinical signs resolved rapidly at 14 dpi. Although body weight and blood immune cell changes were transient, immune cell changes in stomach tissues persisted for more than 2 weeks (Figure 1*F* and Figure 2). In particular, macrophage and mast cell numbers rapidly increased in the stomach tissue after viral infection, and these increases were maintained to some extent even after 4 weeks of infection (Figure 1*F* and Figure 2). Additionally, an increase in neutrophils was observed in the convalescence phase at 4 weeks post-infection (Figure 1*F* and Figure 2). However, SARS-CoV-2 did not alter CD4 T cell or eosinophil numbers in the stomach (Figure 1*F* and Figure 2).

Next, we analyzed cytokine expression, which could affect immune cells at 7 dpi (Figure 1*G* and Figure 2). Unexpectedly, most blood serum cytokine levels were unchanged or reduced in SARS-CoV-2-infected mice compared with those in uninfected mice (Figure 3*A*), suggesting that cytokine changes subsided at 7 dpi and that immune cells in the stomach could be induced at an early stage. Only CXCL13 expression was increased in response to SARS-CoV-2 infection at 7 dpi (Figure 1*H*). Overall, SARS-CoV-2 infection did not promote gastric disease but changed the stomach immune cell composition.

SARS-CoV-2 Infection Induces Dynamic Gene Expression Transitions in the Stomach

To analyze the effect of SARS-CoV-2 in more detail, we evaluated gene expression in uninfected and SARS-CoV-2-infected mice. Stomach specimens were obtained at 7 dpi, and RNA sequencing was performed (Figure 4*A*). Although there were no significant pathologic changes, the heat map and multi-dimensional scaling plot indicated that viral infection caused a profound change in RNA expression (Figure 4*B and C*). Levels of more than 1100 genes differed significantly between SARS-CoV-2-infected and uninfected stomach (Figure 4*C*). Additionally, similar changes in immune subsets were additionally observed in the Cibersort analysis based on transcriptomic data (Figure 3*B*).

Notably, the expression of several genes related to metaplasia, including *Slc7all*, *Alpi*, *Dmp1*, *Cftr*, *Cldn4*, *Cdx2*, and *Tff3*, was higher in SARS-CoV-2-infected stomach than in uninfected stomach (Figure 4*D and E*). In line with cytokine array results, *Cxcl13* was one of the most upregulated genes in SARS-CoV-2-infected stomach compared with expression in uninfected stomach (Figure 1*H* and Figure 4*D and E*). In addition, other immune-associated genes, such as *Arg1*, *Cxcl1*, *Il1rn*, and *Il1rl1* (ST2), were significantly different between the groups (Figure 4*D*). Among the downregulated genes following SARS-CoV-2 infection, growth factors, ECL cell markers, hormones, and metabolism-associated genes were identified. Gene set enrichment analysis (GSEA) of differentially expressed genes (DEGs) showed that gene sets related to metaplasia and early gastric cancer were enriched in SARS-CoV-2-infected stomach compared with levels in uninfected stomach (Figure 4*F*). To verify transcriptome results, we performed immunohistochemistry (IHC) for CDX2 and CLDN4, which are well-defined gastric carcinogenesis markers. Consistently, $CDX2^+$ and $CLDN4^+$ cell emergence was distinct in the corpus-antrum junctional cells of SARS-CoV-2-infected mice (Figure 4*G*).

SARS-CoV-2 Exerts a Negative Synergistic Effect With H pylori-induced Gastritis

Based on the transcriptomic data, we investigated whether SARS-CoV-2 exerted a synergistic effect on gastric disease. Hence, we infected K18-hACE2 mice with SARS-CoV-2 before (pre-COVID) and after (post-COVID) *H pylori* inoculation, and the mice were euthanized 20 weeks after *H pylori* infection (Figure 5*A*). Immunostaining showed that spiral-shaped *H pylori* successfully colonized the stomach 4 weeks after inoculation (Figure 5*B*). Twenty weeks after *H pylori* infection, spontaneous chronic gastritis, accompanied by immune cell accumulation and parietal cell loss, was prominent in the corpus-antrum junction (Figure 5*C*). However, gastritis was more severe in both the pre-COVID and post-COVID groups than in *H pylori*-infected mice (Figure 5*C*). In particular, several indicators involving a thickened mucosa, immune cell infiltration in the submucosa, and signet ring-like cell emergence were more prominent in post-COVID mice than in control mice (Figure 5*C and D*). Although the disease was more severe in pre-COVID mice than in *H pylori*-infected mice, the worst outcomes were observed in post-COVID mice among the 3 models (Figure 5*A, C, and D*). However, in contrast to that in pre-COVID mice, there was no body weight loss due to SARS-CoV-2 infection in post-COVID mice (Figure 5*E*).

To determine whether SARS-CoV-2 affects *H pylori* colonization, we compared the bacterial contents of the stomach specimens between mice infected with bacteria and

Figure 1. (***See previous page***). **Tracing of SARS-CoV-2-infected mice based on the stomach and lung.** *(A)* Image showing the experimental scheme for SARS-CoV-2 infection in K18-hACE2 mice. *(B–C)* Representative histopathologic and *in situ* hybridization images of the lungs and stomach of SARS-CoV-2-infected K18-hACE mice at 2 days, 5 days, 7 days, 14 days, and 4 weeks post-viral infection. Scale bars: 200 mm (panels in *B*); 100 mm (panels in *C*). *(D)* Body weight loss in SARS-CoV-2-infected K18-hACE2 mice (n = 4) and uninfected control mice (n = 4). The percentage (%) represents the rate of loss compared with the initial body weight. *P*-values were obtained by performing the 2-tailed unpaired Student *t*-test (***P* < .01). *(E)* The graph indicates the contents of immune cells in the blood depending on the days post-viral infection. *P*-values were obtained via a 2-way ANOVA multiple comparisons test (n = 4 per group, **P* < .05; ***P* < .01; ****P* < .001). *(F)* The graph indicates the number of immune cells in the stomach based on a 20× high-power field (n = 4 per group). *(G–H)* Gray-scale images show representative images of cytokine arrays based on serum samples from uninfected and SARS-CoV-2-infected mice 7 days after SARS-CoV-2 infection, and the graph indicates the selected cytokines that were differentially expressed. *P*-values were obtained by performing a 2-tailed unpaired Student *t*-test (n = 3 per group, **P* < .05; ***P* < .01; ****P* < .001). All data are presented as the mean ± SEM.

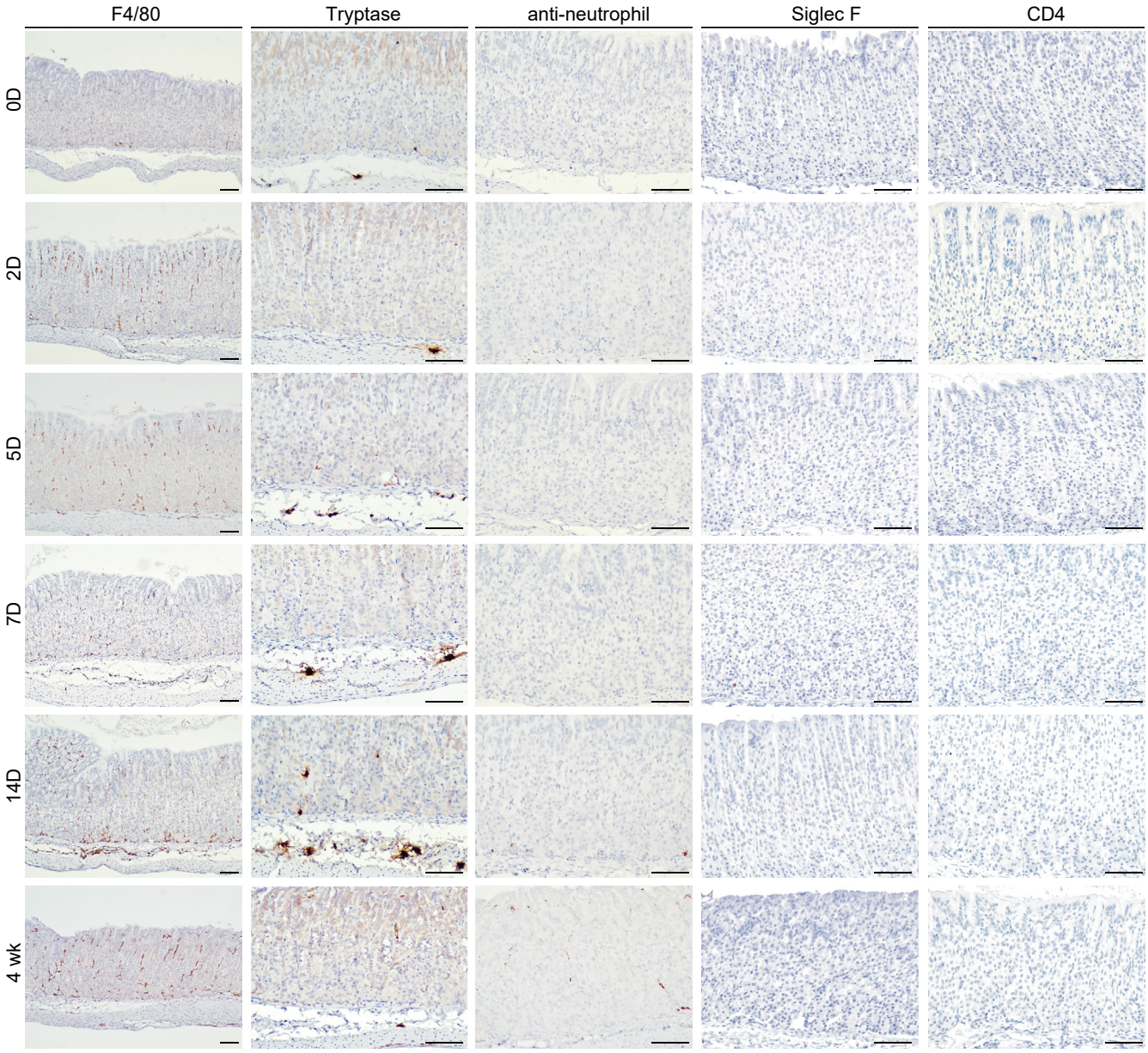

Figure 2. Representative immunohistochemistry images for macrophages (F4/80), mast cells (tryptase), neutrophils (anti-neutrophil), eosinophils (Siglec F), and CD4 T cells (CD4) in SARS-CoV-2 infected K18-hACE mice at 2 days, 5 days, 7 days, 14 days, and 4 weeks post-viral infection. '0D' represents uninfected mice. Scale bars, 100 mm.

those co-infected with bacteria and viruses. SARS-CoV-2 infection did not change this bacterial content, and *H pylori* successfully colonized the stomach, as seen in control mice (Figure 5*F*). These results suggest that the increased gastritis severity in pre-COVID and post-COVID groups are not associated with the number of *H pylori* residing in the gastric gland.

Gastric Lineage Changes in SARS-CoV-2- and H pylori*-infected Mice*

To evaluate gastric disease severity in pre-COVID and post-COVID mice, we first conducted IHC for corpus lineage and proliferating cells affected by *H pylori* infection. As expected, 20 weeks of *H pylori* infection in the stomach elicited distinct histologic changes, including oxyntic atrophy (parietal cell loss), chief cell marker loss (MIST1), foveolar cell hyperplasia, and an increase in proliferating cells, in K18-hACE2 mice (Figure 6*A–E*). In post-COVID mice, $ATP4A^{+}$ parietal cell numbers were significantly lower than those in *H pylori*-infected mice, whereas there was no obvious change in pre-COVID mice (Figure 6*A and B*). Notably, parietal cell loss, which is primarily induced during chronic inflammation, differed depending on the timing of SARS-CoV-2 infection (Figure 6*B*). Meanwhile, $MIST1^{+}$ cell ablation and an increase in $MUC5AC^{+}$ foveolar cells were prominent in both post- and pre-COVID mice compared with

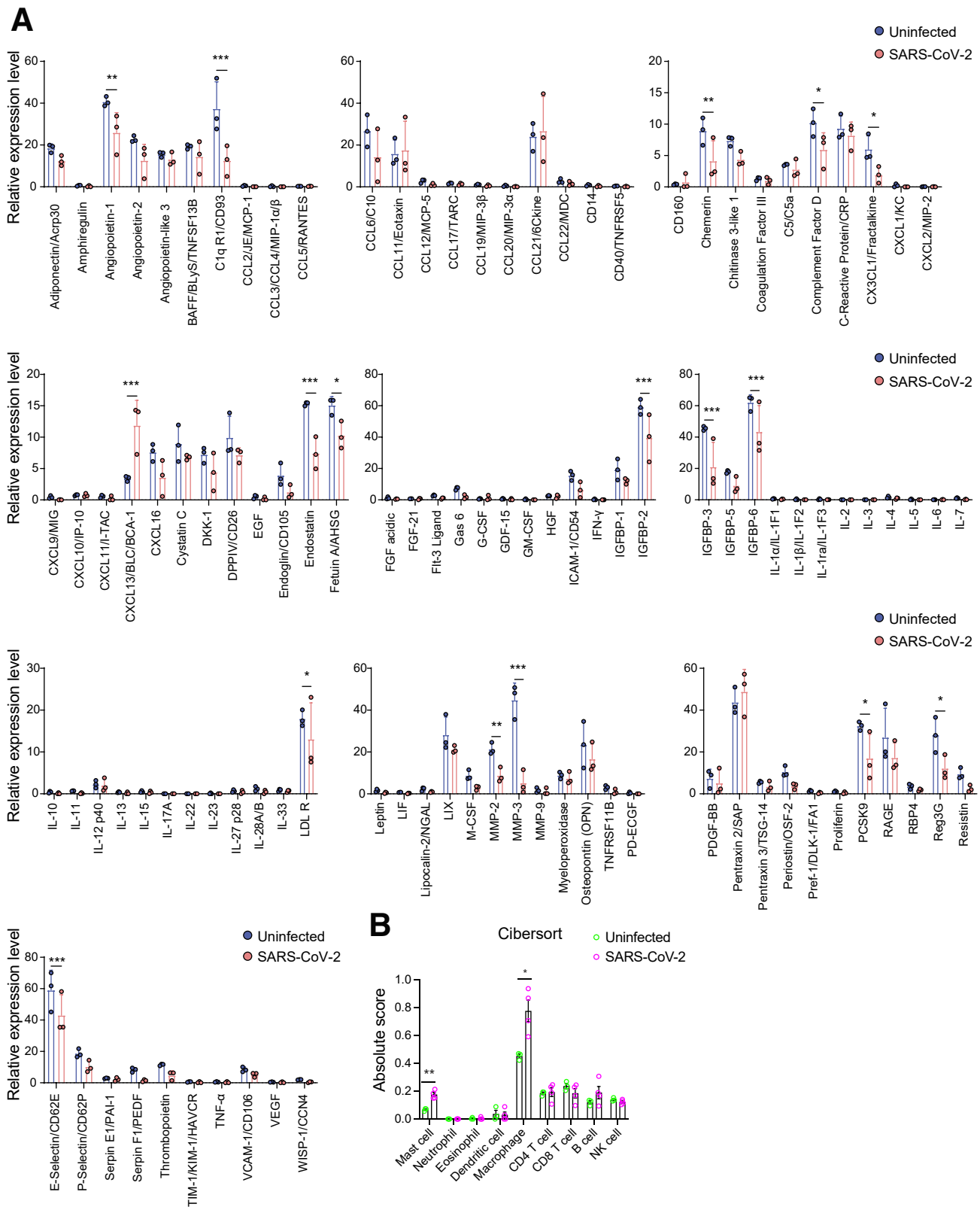

Figure 3. Evaluation of cytokines and immune subsets in mice after COVID-19. *(A)* Graphs showing the cytokine array data using serum samples from uninfected and SARS-CoV-2-infected mice 7 days after SARS-CoV-2 infection. Both significantly changed and unchanged cytokines are represented. *P*-values were obtained by performing a 2-tailed unpaired Student *t*-test (n = 3 per group, $^{*}P < .05$; $^{**}P < .01$, $^{***}P < .001$). *(B)* Graph showing the predicted proportion of immune cells in the mouse stomach (n = 3–4 per each group). The "Absolute Score" was estimated as the median expression level of all genes in the signature matrix divided by the median expression level of all genes in the mixture. *P*-values were obtained by performing a 2-tailed unpaired Student *t*-test ($^{*}P < .05$; $^{**}P < .01$). All data are presented as the mean ± SEM.

observations in *H pylori* mice (Figure 6*A, C, and D*). Overall, the degree of changes in corpus lineages was more radical in post-COVID mice than in pre-COVID mice. In contrast, SARS-CoV-2 infection caused a similar increase in MKI67^{+} proliferating cells in *H pylori*-infected mice, regardless of the viral infection time (Figure 6*A and E*).

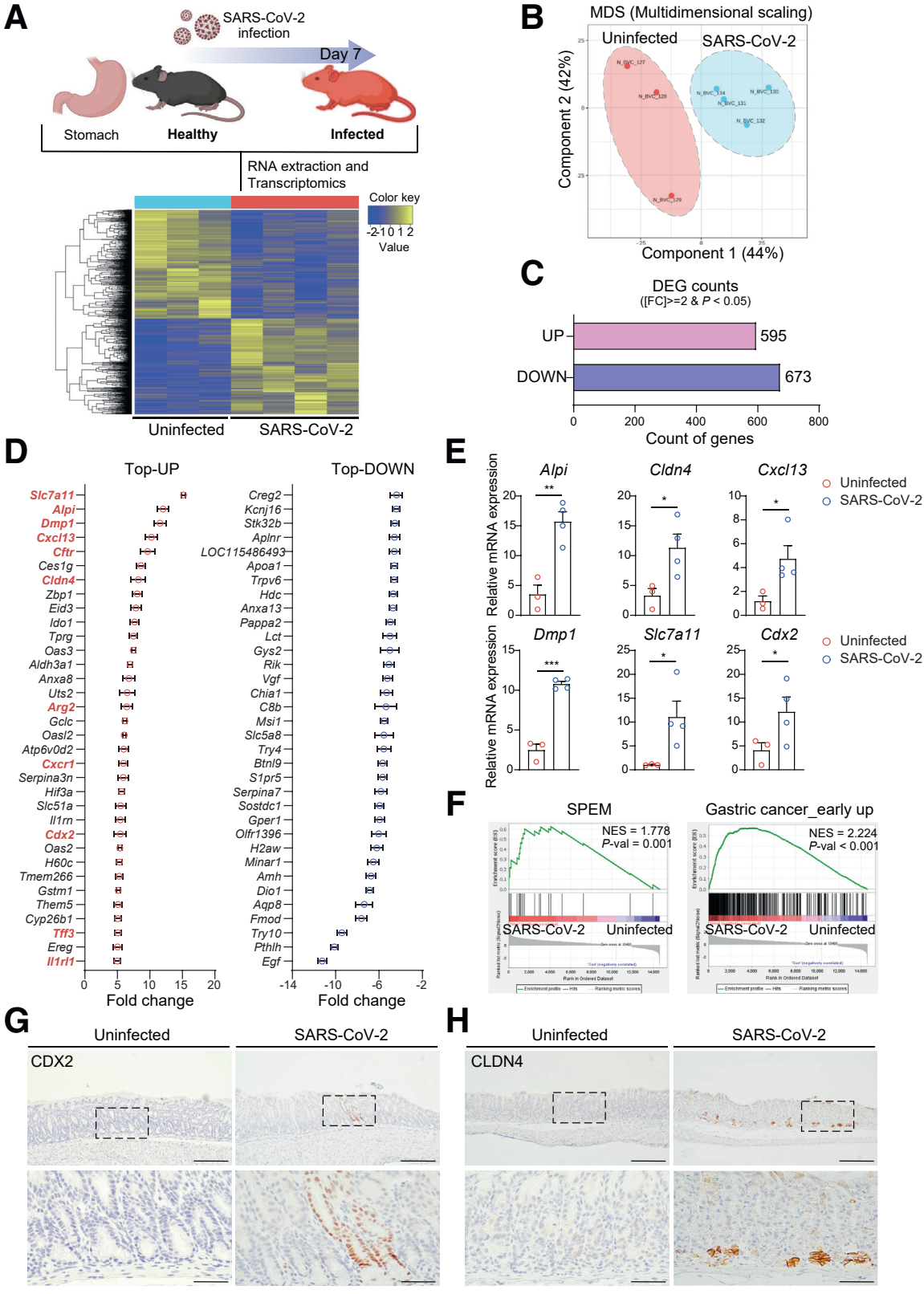

SARS-CoV-2 Strengthens the Chronic Inflammatory Response in H pylori*-infected Mice*

We then conducted transcriptomics using stomach specimens from post-COVID mice to explore the altered molecular profiles. This analysis of *H pylori* and post-COVID groups revealed that immune-related gene sets were altered and among the top 10 gene ontology terms (Figure 7*A*). This was consistent with the histologic features of post-COVID mice, characterized by more immune cells in the gland base and submucosal region (Figure 7*C*). Among the immune-related pathways, IL6/JAK_STAT3, IFNg, and IL2_STAT5 signaling, which can lead to chronic responses, were significantly and positively enriched in post-COVID mice compared with levels in control mice (Figure 8*A, C, and D*). In addition, the immunological gene set associated with preneoplastic metaplasia was also changed in post-COVID mice compared with levels in *H pylori*-infected mice (Figure 7*B*).

Because the immune response following *H pylori* infection can stimulate different inflammatory cells related to disease progression, we investigated which immune subsets were affected by SARS-CoV-2 in the *H pylori*-infected gastritis model. As expected, *H pylori* infection caused a dramatic increase in innate and adaptive immune cell numbers (Figure 7*C–H*, and Figure 9*A and B*). Notably, increased patterns of macrophages and mast cells, modulated upon infection with SARS-CoV-2 alone, were maintained in pre-and post-COVID mice (Figure 1*F* and Figure 7*C, E, and H*). In addition, $CD4^+$ T cell numbers were higher in post-COVID mice than in *H pylori*-infected mice (Figure 7*C and D*). However, SARS-CoV-2 did not affect neutrophils or eosinophils in the *H pylori*-induced gastritis model (Figure 7*F, G*, and Figure 9*A and B*). Together, SARS-CoV-2 infection elicits a strengthened inflammatory response in *H pylori*-infected mice.

Aggravated premalignant Condition in Pre- and Post-COVID Mice

During gastric carcinogenesis, *H pylori* infection promotes stepwise progression involving oxyntic atrophy, chronic inflammation, preneoplastic metaplasia, and eventually cancer. To determine whether a strengthened immune response can contribute to disease progression in SARS-CoV-2-co-infected mice, we assessed premalignant conditions in *H pylori*-infected pre- and post-COVID mice based on CD44v9 and GSII or MKI67, which are metaplasia and proliferation markers, respectively (Figure 10*A*). Immunofluorescence images indicated that $CD44v9^+$/$GSII^+$ metaplastic cells emerged from the basal region of the gland after *H pylori* infection, and metaplastic cell numbers were remarkably elevated in post-COVID mice compared with those in *H pylori*-infected mice (Figure 10*A and B*). Notably, preneoplastic cells expanded into the entire gland in post-COVID mice (Figure 10*A*). Albeit not to the same extent as that in post-COVID mice, metaplastic cell numbers in pre-COVID mice were slightly increased (Figure 10*A and B*). Consistently, $GSII^+$/$MKI67^+$ proliferating metaplastic cells were also increased in pre- and post-COVID mice compared with numbers in *H pylori*-infected controls (Figure 10*A and C*).

Notably, disease progression-associated gene sets involving the epithelial-mesenchymal transition were significantly enriched in post-COVID mice compared with levels in *H pylori*-infected controls (Figure 8*B* and Figure 10*D*). In addition, GSEA results showed positive enrichment scores in pathways associated with E2F targets and KRAS signaling in post-COVID mice compared with levels in *H pylori*-infected controls, supporting the increase in metaplasia and proliferating cells (Figure 8*B*). In line with the transcriptomic analysis results, levels of p-STAT3 and p-ERK, which are pivotal for disease progression,[33–35] were evident and elevated in the gastric lesions of co-infected mice compared with those of *H pylori*-infected mice (Figure 8*C and D*). Previously, we described the role of WFDC2, which promotes preneoplastic metaplasia and serves as an effective prognostic marker and putative target in gastric cancer.[19] Hence, we explored changes in *Wfdc2* expression in K18-hACE2 mice. Co-infection with SARS-CoV-2 and *H pylori* resulted in increased expression in the corpus-antrum junction, where gastritis and chronic inflammation were observed (Figure 10*E and F*). Collectively, our findings suggest that SARS-CoV-2 infection strengthens the immune response and promotes adverse premalignant conditions in response to *H pylori* infection.

Discussion

Long COVID comprises a wide range of new, returning, or ongoing health problems experienced after infection with the COVID-19-causing virus. Emerging research suggests that the GI tract exhibits morbidities after the acute COVID-19 phase[8,9,11] and that gut microbiomes might undergo crosstalk with SARS-CoV-2.[36,37] Despite advances in our

Figure 4. (***See previous page***). **Dynamic changes in gene expression after SARS-CoV-2 infection in the stomach.** *(A)* Schematic image showing the experimental scheme of transcriptomics using stomach specimens from K18-hACE2 mice (n = 4) at 7 days post-SARS-CoV-2 infection. Healthy uninfected mice (n = 3) inhaled the vehicle. Heatmap showing DEGs between the groups. *(B)* Multi-dimensional scaling plot of transcriptomics of uninfected and SARS-CoV-2-infected mice. *(C)* Graph showing the number of significantly upregulated and downregulated genes from transcriptomic data comparing uninfected and SARS-CoV-2-infected mice. The genes were selected based on a fold-change greater than 2 and a *P*-value less than .05. *(D)* List of top upregulated and downregulated genes in SARS-CoV-2-infected mice compared with levels in uninfected mice. *(E)* mRNA expression of *Alpi*, *Cldn4*, *Cxcl13*, *Dmp1*, *Slc7a11*, and *Cdx2* in the stomach of uninfected and SARS-CoV-2-infected mice. *P*-values were obtained by performing a 2-tailed unpaired Student *t*-test (n = 3–4 per group, $^*P < .05$; $^{**}P < .01$; $^{***}P < .001$). The expression levels are normalized to those of *Gapdh*. *(F)* GSEA comparing uninfected mice and SARS-CoV-2-infected mice. *(G–H)* Representative IHC images for CDX2 and CLDN4 expression in uninfected and SARS-CoV-2-infected mice. Scale bars, 200 mm (*upper panels*), 100 mm (*lower panels*). All data are presented as the mean ± SEM.

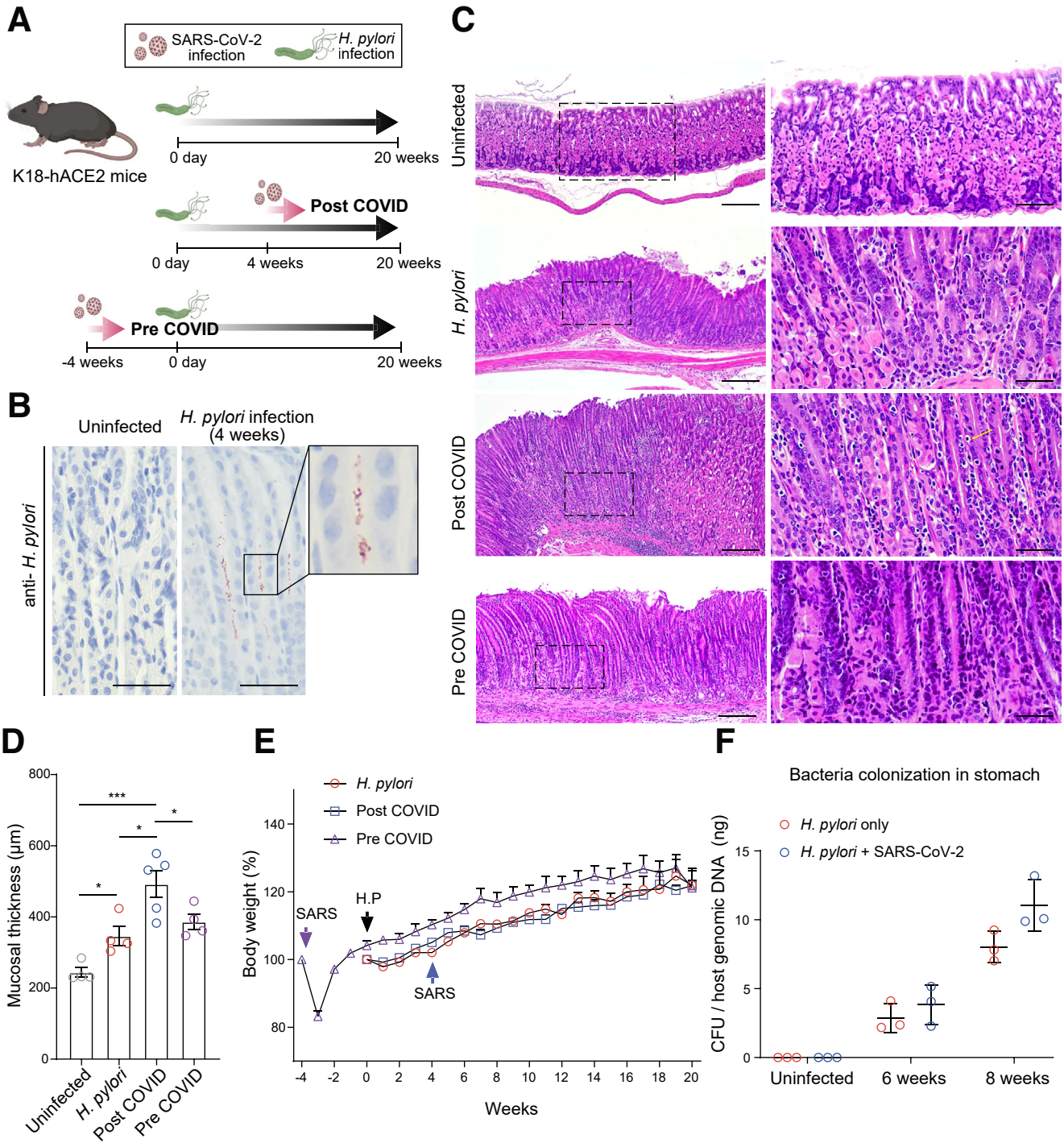

Figure 5. Negative synergistic effect of SARS-CoV-2 on *Helicobacter pylori*-induced chronic gastritis. *(A)* Image showing the experimental scheme of the 3 infection models using SARS-CoV-2 and *H pylori*. *Model at the top*: *H pylori*, K18-hACE mice infected only with *H pylori*; *model in the middle*, post-COVID, K18-hACE2 mice infected with SARS-CoV-2 4 weeks after *H pylori* inoculation; *model at the bottom*; pre-COVID: K18-hACE2 mice infected with SARS-CoV-2 4 weeks before *H pylori* inoculation. *(B)* Representative IHC images for *H pylori* in K18-hACE2 mice after 4 weeks of bacterial inoculation and in uninfected mice. Scale bars, 50 mm. *(C)* Representative H&E-stained images of the stomach of uninfected, *H pylori*, post-COVID, and pre-COVID groups. Scale bars, 200 mm (*left panels*); 50 mm (*right panels*). The *yellow arrow* indicates clear cells with pale cytoplasm. *(D)* The graph indicates the gastric mucosal thickness in the uninfected, *H pylori*, post-COVID, and pre-COVID groups. *P*-values were obtained by 1-way ANOVA multiple comparisons test (n = 4–5 per group, $^{*}P < .05$; $^{***}P < .001$). *(E)* Body weight loss for *H pylori*, post-COVID, and pre-COVID groups. The percentage (%) represents the rate of loss compared with the initial body weight. 'SARS' indicates the date of viral infection and 'H.P' indicates the date of bacterial inoculation. *(F)* Quantification results for *H pylori* colonization in stomach specimens of SARS-CoV-2- and *H pylori*-co-infected mice (n = 3 per group) and uninfected mice (n = 3). The bacterial number was normalized to host genomic DNA using *GAPDH* expression. All data are presented as the mean ± SEM.

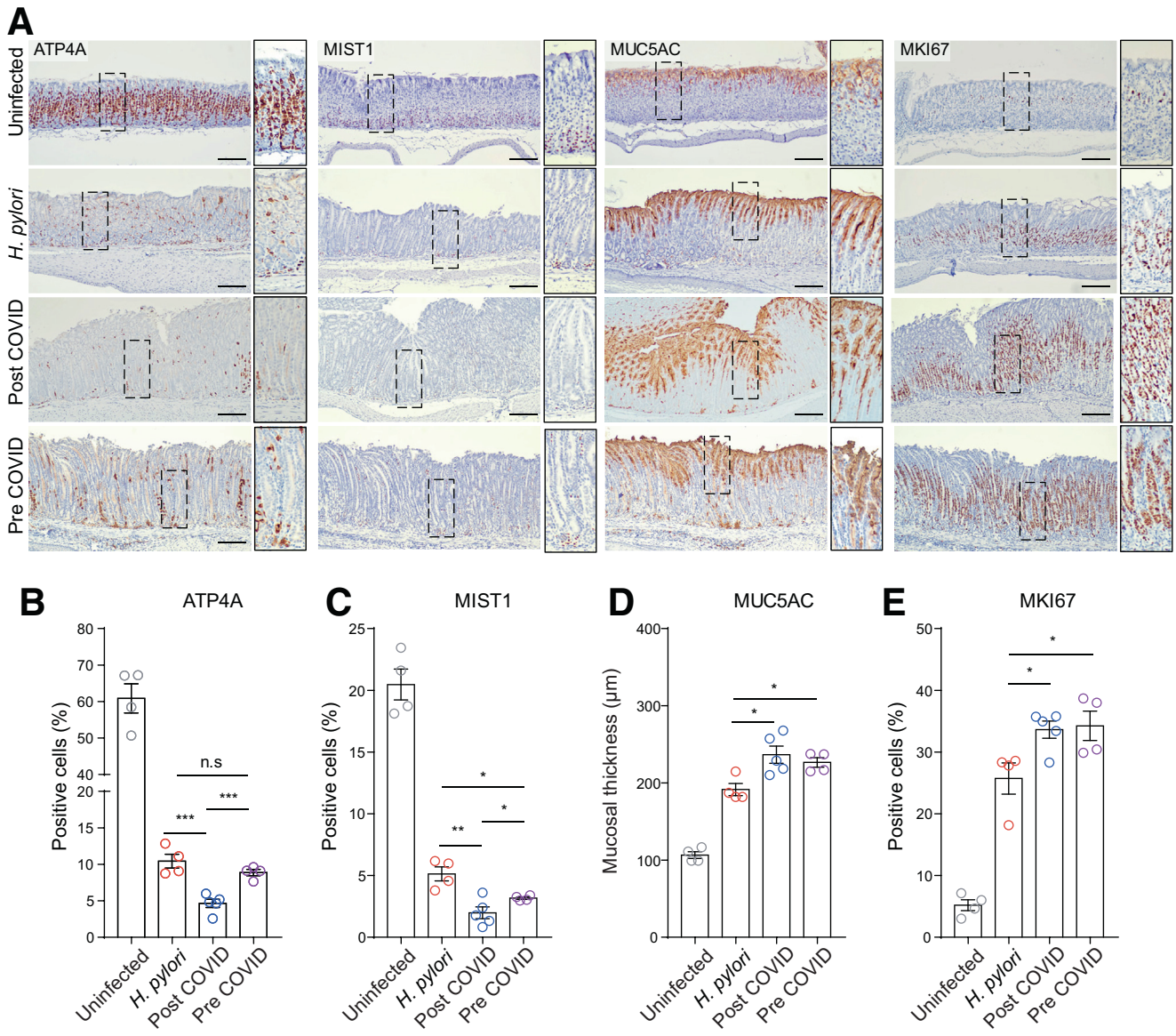

Figure 6. Assessment of changes in the corpus lineage and proliferating cells in pre- and post-COVID mice. *(A)* Representative IHC images for the corpus cell lineage (ATP4A, MIST1, MUC5AC) and proliferating cells (MKI67) in uninfected, *Helicobacter pylori*, post-COVID, and pre-COVID groups. Scale bars, 200 mm. *(B–D)* The graphs indicate the percentage of ATP4A-, MIST1-, and MKI67-positive cells to total cells based on 10× high-power fields. The average MUC5AC-positive length was measured from the gland top (0 mm). *P*-values were obtained by 1-way ANOVA multiple comparisons test (n = 4–5 per group, **P* < .05; ***P* < .01; ****P* < .001). All data are presented as the mean ± SEM.

understanding of the post-acute sequelae of COVID-19, limited studies have examined the stomach. In this study, we performed RNA sequencing of stomach specimens from K18-hACE mice after SARS-CoV-2 inhalation. Transcriptomic data indicated that more than 1100 genes were significantly altered in the stomach during the acute COVID-19 phase. The most altered immune cells and genes were associated with the development of gastric lesions. Most importantly, SARS-CoV-2 and *H pylori* co-infection exacerbated disease progression.

The relationship between non-inflammatory GI symptoms and COVID-19 remains controversial.[26,27,38,39] However, here, SARS-CoV-2 infection exerted a negative synergistic effect on inflammation-prone disease in the stomach. In this regard, there are some possibilities that can be suggested. First, unlike previous studies, which have suggested that the microbiome can reduce *H pylori* colonization,[40] we observed that *H pylori* colonization was not affected by SARS-CoV-2 co-infection. Second, although the co-infection of gastric epithelial cells by *H pylori* and SARS-CoV-2 could theoretically lead to adverse outcomes, our data showed that SARS-CoV-2 does not directly infect gastric cells. Instead, it indirectly alters the epithelial cell molecular characteristics associated with pre-cancer progression. Third, whereas COVID-19 may influence translocation of the *H pylori* CagA oncoprotein via the Type 4

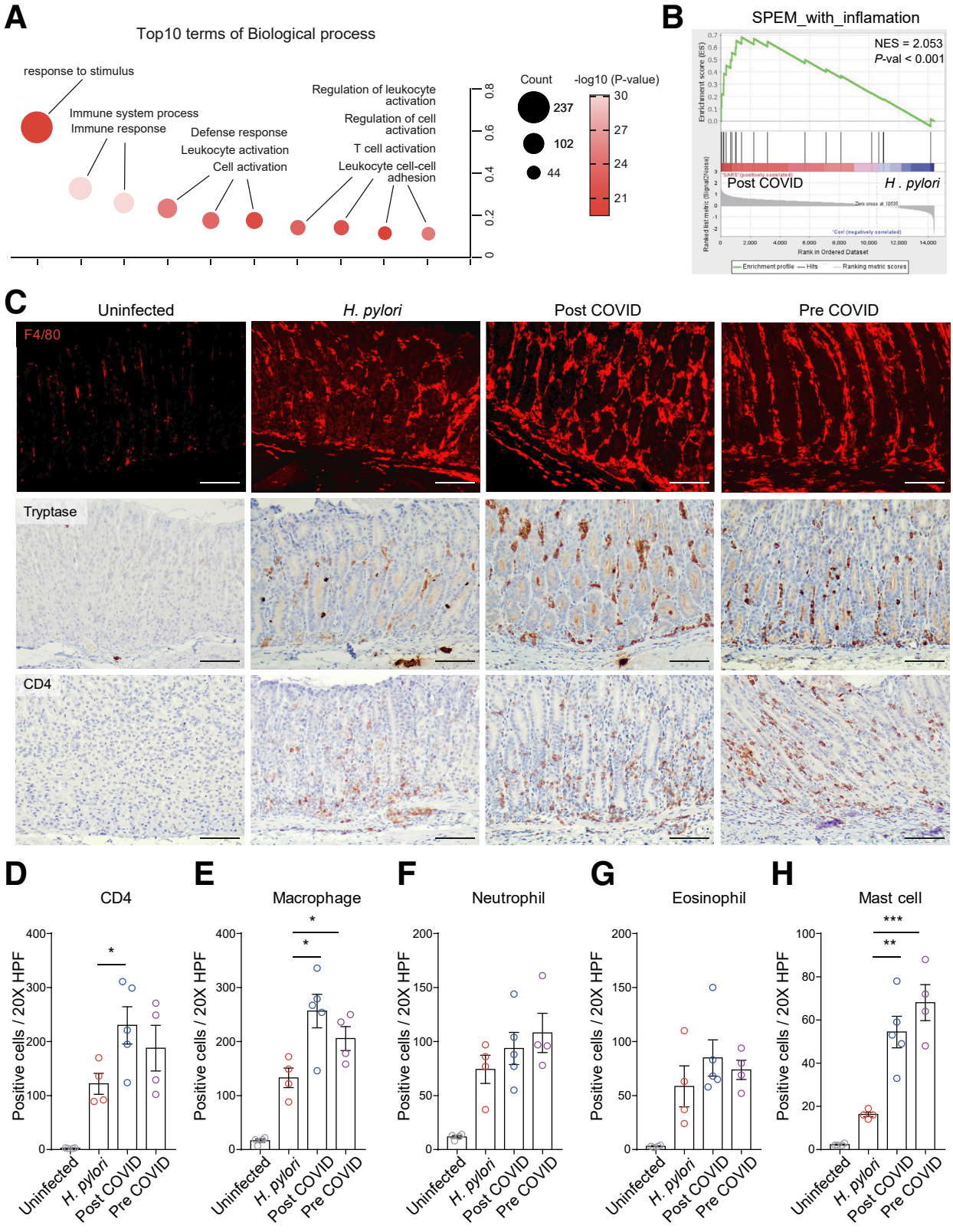

Figure 7. Enhancement of specific immune subsets in post-COVID mice. *(A)* Bubble plot showing the selected top 10 terms from the gene ontology functional analysis of transcriptomic data comparing *Helicobacter pylori*-infected and post-COVID mice. Significance was derived from the Fisher exact test. *(B)* GSEA comparing *H pylori* and post-COVID groups. *(C)* Representative immunofluorescence and IHC images for macrophages (F4/80), mast cells (tryptase), and CD4 T cells (CD4) in uninfected, *H pylori*, post-COVID, and pre-COVID groups. Scale bars, 100 mm. *(D–H)* Graphs indicating the number of immune cells in 20× high-power fields. *P*-values were obtained by 1-way ANOVA multiple comparisons test (n = 4–5 per group, $^{*}P < .05$; $^{**}P < .01$; $^{***}P < .001$). All data are presented as the mean ± SEM.

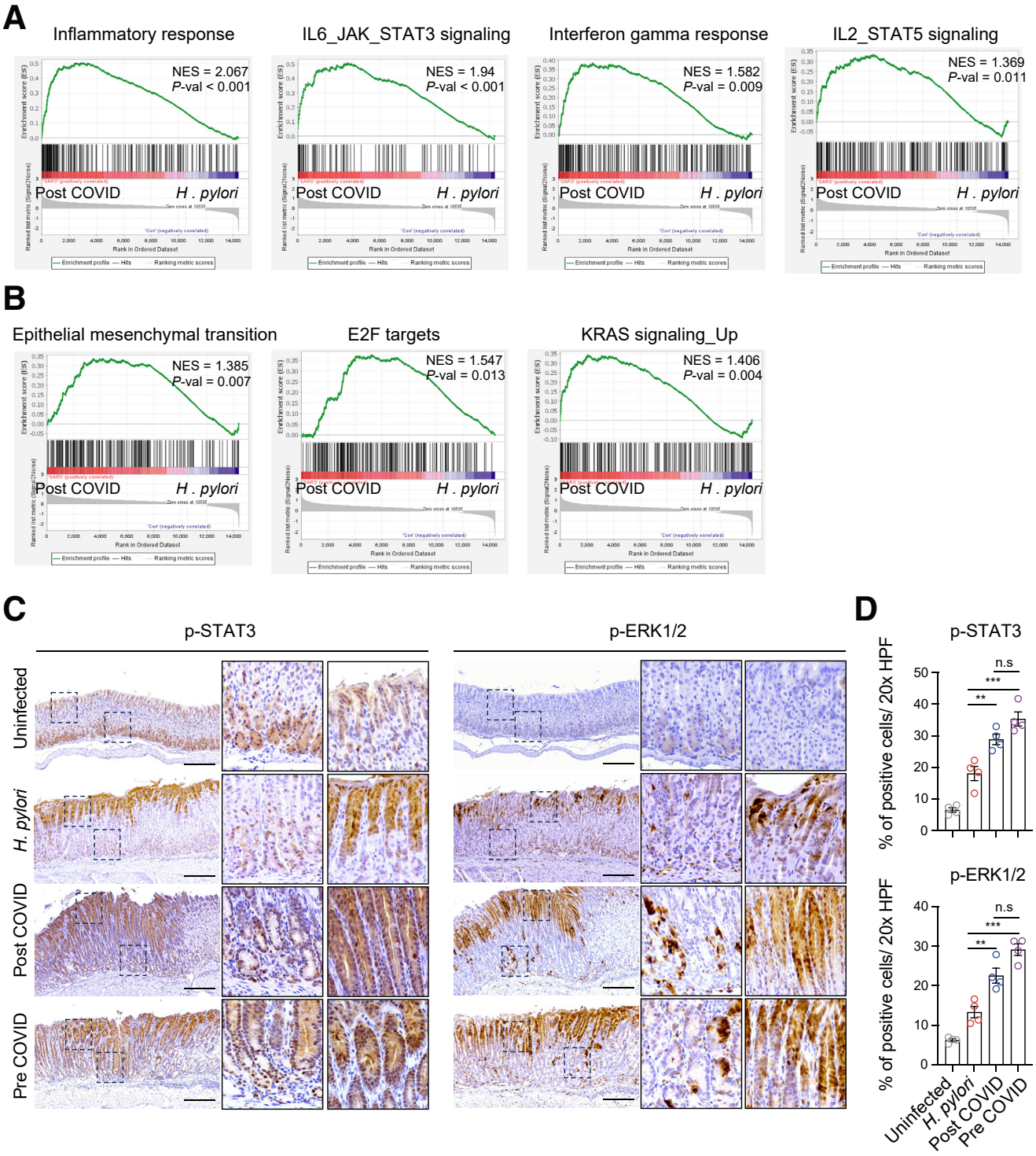

Figure 8. Alteration in disease-associated genes in Post-COVID mice. *(A–B)* GSEA of immune-related and disease progression-related gene sets comparing *Helicobacter pylori* and post-COVID groups. *(C)* Representative IHC images for p-STAT3 and p-ERK1/2 in uninfected, *H pylori*, post-COVID, and pre-COVID groups. Scale bars, 200 μm. *(D)* The graphs indicate the percentage of p-STAT3- and p-ERK1/2-positive cells among total cells based on 20× high-power fields. *P*-values were obtained via a 1-way ANOVA multiple comparisons test (n = 4 per group, $^{**}P < .01$; $^{***}P < .001$).

secretion system (T4SS), the non-functional T4SS of the *H pylori* SS1 strain used in our study suggests that this is unlikely in our model. However, macrophages and mast cells, which are distinct components of *H pylori*-induced gastritis,[22,41] were more abundant in the stomach following SARS-CoV-2 infection. In conclusion, we suggest that SARS-

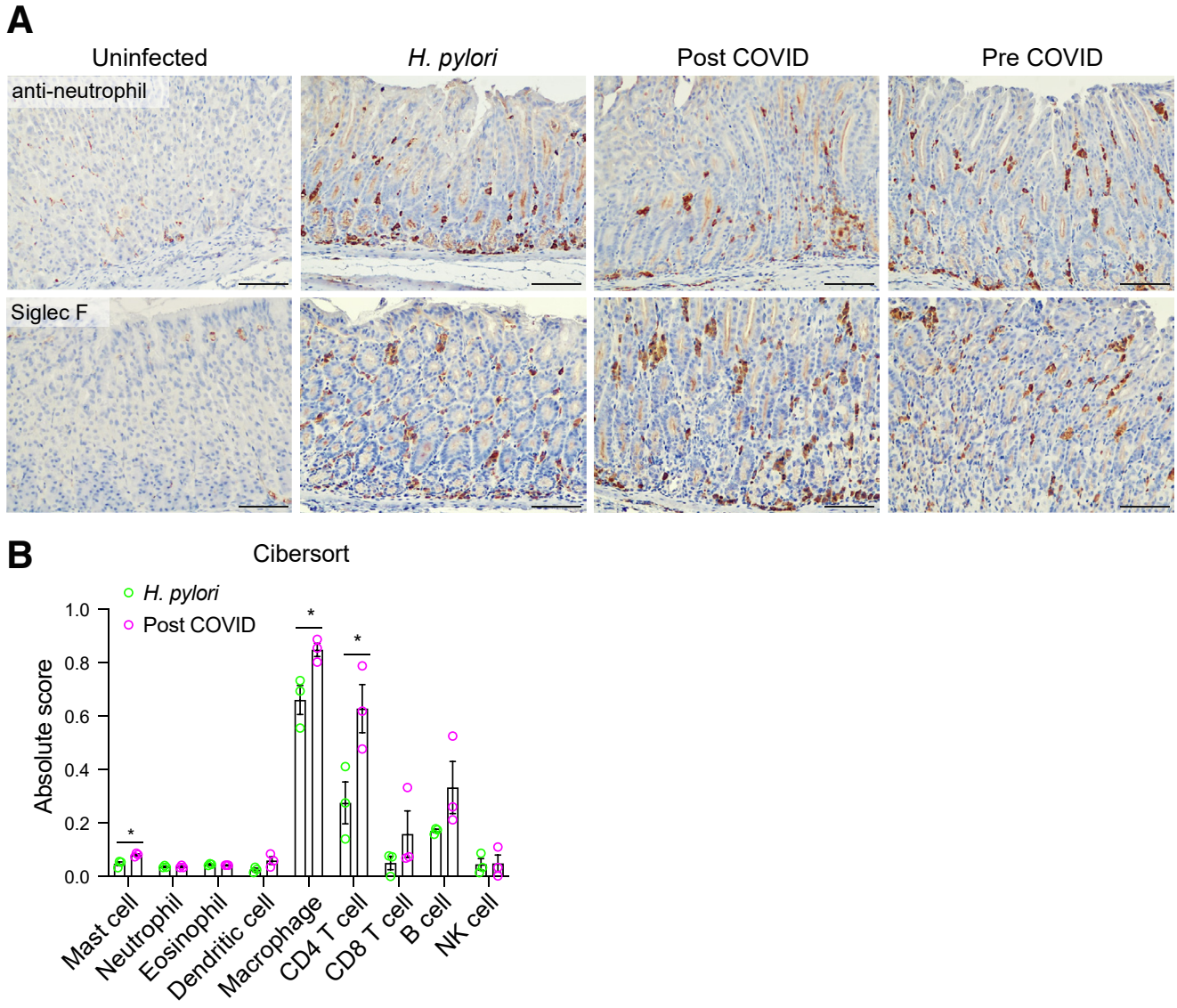

Figure 9. Assessment of immune subsets using IHC and Cibersort analysis. *(A)* Representative IHC images for neutrophils (anti-neutrophil) and eosinophil cells (Siglec F) in uninfected, *H pylori*, post-COVID, and pre-COVID groups. Scale bars, 100 mm. *(B)* Graphs showing the predicted proportion of immune cells in the mouse stomach (n = 3 per each group). The "Absolute Score" was estimated as the median expression level of all genes in the signature matrix divided by the median expression level of all genes in the mixture. *P*-values were obtained by performing a 2-tailed unpaired Student *t*-test (*$P < .05$). All data are presented as the mean ± SEM.

CoV-2 infection elicits a synergistic effect with *H pylori* by promoting changes in the molecular characteristics of gastric cells and leading to an increase in the deposition of specific immune subsets in the stomach.

Most patients with COVID-19 improve within a few days to a few weeks after viral infection; therefore, at least 4 weeks after infection represents the time at which long COVID could be first identified. For extended long COVID-19 research on the stomach, we utilized the K18-hACE2 mice used in our previous research on the lungs.[3,42] To avoid mortality and mimic the convalescence phase in human patients, we subjected animals to SARS-CoV-2 inhalation instead of using the previous intranasal method. Notably, we also divided the mice into pre-COVID and post-COVID groups, since human patients are rarely simultaneously infected with 2 different microorganisms. Recovery traits marked by a reduction in inflammatory foci were identified in the lungs at 4 weeks post-SARS-CoV-2 infection, but changes in immune subsets in the stomach remained even after viral particle removal. This suggests that the effects of SARS-CoV-2 infection on the stomach persist to some extent beyond the post-acute COVID-19 phase. Supporting this, pre-COVID mice exhibited significant alterations, including the loss of parietal cells, loss of chief cell markers, and an increase in metaplastic cells, compared with observations in *H pylori*-infected control mice. Likewise, the immune

subsets affected by SARS-CoV-2 infection were still enriched in the co-infected mice (Figure 1*F* and Figure 7). Because macrophages and mast cells can promote gastric inflammation and initiate gastric tumorigenesis, these pre-established subsets might accelerate gastric disease in co-infected mice.[22,43,44]

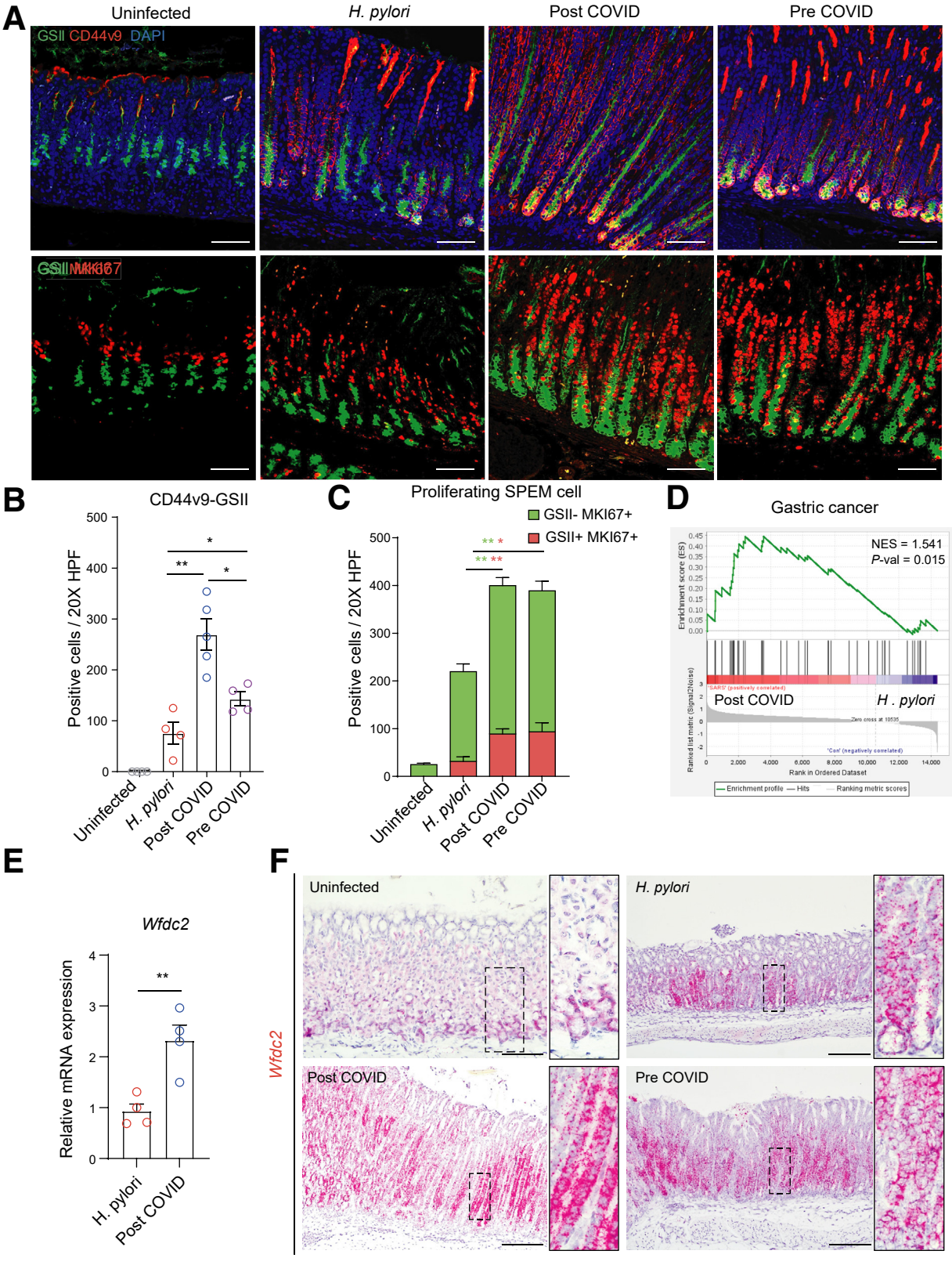

Over one-half of the global population is infected with *H pylori*, meaning that not everyone with an *H pylori* infection develops gastric cancer. Nevertheless, the importance of *H pylori* in gastric carcinogenesis cannot be ignored.[45,46] Various factors, including genetic diversity, dietary habits, and tobacco use, seem to define *H pylori* pathogenicity. Also, these etiological factors appear to be associated with other microbial communities. Sgouras et al revealed that *Lactobacillus* spp. suppress chronic gastritis by inhibiting *H pylori* colonization.[40] EBV positivity is also associated with *H pylori*-induced gastritis severity and gastric cancer development.[31,32,47] Pryia Saju et al found that EBV can suppress the host response to *H pylori* by mediating *SHP-1* methylation. However, here, SARS-CoV-2 infection did not affect *H pylori* colonization. Instead, SARS-CoV-2 induced profound alterations in the molecular profile related to gastric carcinogenesis. Previous results suggest that the most upregulated (*Slc7a11*, *Dmp1*, *Cxcl13*, *Cftr*, *Cldn4*) and downregulated gene sets (*Chia1*) in our transcriptomic data contribute to preneoplastic metaplasia, intestinalization, and cancer development, serving as prognostic markers for gastric cancer.[16,48–51] Especially, $CDX2^{+}$ cell emergence in the corpus-antrum junction was noteworthy, because CDX2 was suggested to be a master transcription factor involved in pre-cancer development by enhancing intestinal markers, such as *Muc2*, *Tff3,* and *Alpi*, and subsequently promoting this disease with additional mutations.[21,52] Hence, CDX2 likely plays a crucial role in accelerating premalignancy in these mice. However, whether CDX2 is the most crucial molecule involved in the dynamic and post-acute COVID-19-associated changes in the stomach is unclear. We assume that a robust inflammatory response derived from the primary infection site can initially and indirectly affect stomach cells.

This study has some limitations. Owing to the high prevalence of *H pylori* and SARS-CoV-2 in South Korea, specimens without a history of infectious disease are extremely rare. Therefore, we were unable to provide comparative transcriptomic data for humans. In addition, we did not observe a direct interaction between gastric cancer and COVID-19. Although many researchers have attempted to establish gastric cancer-model mice, an appropriate cancer model resembling that of human patients has not been developed. Choi et al established transgenic mice expressing the *Mist1*-CreERT2-inducible mutated KRAS (G12D).[34] They generated transgenic mice based on human data, and the mice developed dysplasia that effectively mimicked the molecular features shown in human patients,[20] suggesting that KRAS has an oncogenic function during gastric carcinogenesis. However, these mice did not develop gastric adenocarcinoma. Furthermore, model mice must express K18-hACE2 to conduct COVID-19 research; however, we purchased all hACE2 male mice from the Jackson laboratory. Owing to issues related to interest and the lack of a gastric cancer model, we could not provide direct evidence for this and only could use male mice. However, we found that levels of KRAS, epithelial-mesenchymal transition, and E2F target gene sets were upregulated in the mice. Along with transcriptome changes, the number of metaplastic and proliferating cells was increased in post-COVID mice. Consistent with this, WFDC2, which was previously suggested to be related to gastric cancer prognosis, was prominently expressed in post-COVID mice.[19]

When looking at the overall phenomenon, stomach cells exposed to SARS-CoV-2 resemble a "loaded gun." Protein levels do not seem to perfectly mimic RNA levels, which are remarkably elevated after viral infection. Nevertheless, cells positive for CDX2 and CLDN4 proteins were enriched in the corpus-antrum junction, where chronic gastritis primarily occurred. The potential for deterioration of stomach cells post-COVID seems to increase markedly when they encounter other triggers, such as *H pylori*. Collectively, our findings provide a putative pathogenic mechanism in the stomach in the post-COVID era and imply that co-infection with SARS-CoV-2 and the pathogenic microbiome might be related to gastric disease progression and prognosis. Thus, this study provides significant evidence regarding the risk of severe chronic gastritis in the post-COVID-19 era.

Methods

Animals

Male K18-hACE mice (Tg [K18-ACE2] 2 Prlmn/J) with a C57BL6 background were purchased from Jackson Laboratory. Because only male mice are commercially available, all experiments were conducted using male mice. Animal experiments were performed at the Animal Biosafety Level 3 (ABL3) facility in accordance with the Public Health Service Policy on Human Care and Use of Laboratory Animals. Animals were randomly divided into 3 groups, using a computer-based random generator. All procedures were approved by the Institutional Animal Care and Use Committee (IACUC: 2020-0216) of Yonsei University College of Medicine and accredited by the Association for Assessment and Accreditation of Laboratory Animal Care International (#001071). In accordance with safety guidelines, all animal experiments were performed in the ABL3 facility, and all samples were allowed to leave the ABL3 facility following DNA and RNA protein extraction or fixation procedures to

Figure 10. (***See previous page***). **Molecular characterization of post-COVID mice defines an increased risk of gastric lesions.** *(A)* Representative immunofluorescence images for GSII, CD44v9, and MKI67 expression in uninfected, *Helicobacter pylori*, post-COVID, and pre-COVID groups. Scale bars, 100 mm. *(B–C)* Graphs indicating the number of preneoplastic cells in 20× high-power fields. *P*-values were obtained by performing 1-way ANOVA multiple comparisons test (n = 4–5 per group, $^{*}P < .05$; $^{**}P < .01$). *(D)* GSEA comparing *H pylori*-infected and post-COVID mice. *(E)* mRNA expression of *Wfdc2* in the stomach of *H pylori*-infected and post-COVID mice. *P*-values were obtained by performing a 2-tailed unpaired Student *t*-test (n = 4 per group, $^{**}P < .01$). *(F)* Representative *in situ* hybridization images for *Wfdc2* in uninfected, *H pylori*, post-COVID, and pre-COVID groups. Scale bars, 100 mm. All data are presented as the mean ± SEM.

avoid SARS-CoV-2 activation. For quantification and obtain significance, we used at least 3 mice for each experiment, and there were no inclusion and exclusion criteria in this study.

Virus Production

Vero cells, a Vero African green monkey kidney cell line (KCLB 10081), were used to produce SARS-CoV-2. Culturing SARS-CoV-2 was obtained from the National Culture Collection for Pathogens of Osong, Korea (NCCP 43326, S type), and virus titer measurements were performed in accordance with our previous study.[3] In brief, SARS-CoV-2 was cultured in Vero cells until a cytopathic effect was observed in >80% of cells. The supernatants were centrifuged at 380 $\times$ g for 15 minutes to remove cell debris, aliquoted, and stored at −80 °C. SARS-CoV-2 stocks and infected tissues were titrated using plaque assays. Vero cells were seeded in a 6-well plate the day before the assay. Serially diluted supernatants or homogenized tissues were then added, and the mixture was incubated for 1 hour with gentle agitation every 15 minutes. The cells were overlaid with Dulbecco's modified Eagle medium containing 1% SeaPlaque agarose (Lonza), 2% fetal bovine serum (FBS), 100 units/mL penicillin, and 100 μg/mL streptomycin. After 3 days, the plaques were cleared, and the cells were fixed with 4% paraformaldehyde and stained with a 0.5% crystal violet–20% methanol solution. The enumerated plaques were used to determine the viral titers.

Mouse Infection With SARS-CoV-2 and H pylori

For SARS-CoV-2 infection, a modified version of the Kent Scientific Chamber Nebulizer Delivery System was used to induce infection via inhalation. K18-hACE2 mice were exposed to 1×10^6 SARS-CoV-2 particles in an isolated chamber for 30 minutes. Uninfected control mice were treated with an equal volume of phosphate-buffered saline (PBS). For infection, *H pylori* was cultured on antibiotic-supplemented *Brucella*-broth containing 10% FBS in a microaerobic jar with a GasPack at 37 °C and a 5% CO_2 incubator. The mice were starved for 12 hours before the first day of *H pylori* infection, and 1×10^8 CFUs of *H pylori* were orally inoculated 3 times at 2-day intervals. For the post-COVID model, 9-week-old mice were initially infected with *H pylori*. After 4 weeks, SARS-CoV-2 was administered via inhalation. In the pre-COVID model, animals were subjected to SARS-CoV-2 inhalation 4 weeks before *H pylori* infection. The total *H pylori* infection period was 20 weeks. For blinding test, the primary investigator, who was the only person aware of the group allocation, infected virus and bacteria to randomized groups, and experiments involving measurement of body weight changes, immune cell changes, and histologic observation were conducted by other investigators who did not know the allocation.

Histopathologic Analysis

For histopathologic analysis, the mice were euthanized at each time point using a CO_2 chamber, and collected tissues were fixed in 10% neutral buffered formalin (Sigma) for 24 hours and embedded in paraffin. Fixed samples were cut into 4 μm-wide slides using a microtome (Leica) for subsequent hematoxylin and eosin (H&E) staining and IHC. For H&E staining, sections were de-paraffinized through 3 immersions in xylene, followed by rehydration in a series of ethanol concentrations (100%, 95%, and 70%). The slides were then stained with 0.1% Mayer's haematoxylin (Agilent) for 10 minutes, followed by immersion in 0.5% Eosin Y (Sigma) solution. The slides were then rinsed in distilled water until eosin streaking stopped and then dehydrated in ascending concentrations of ethanol (50%, 70%, 95%, and 100%) for 1 minute each. The slides were covered with a mounting solution (Thermo) and examined under a light microscope (Olympus BX43). Histopathologic analysis was performed by an experienced animal pathologist (K.T.N.).

In Situ Hybridization

An *hACE2* and *Wfdc2* RNA probe and RNAscope 2.5 HD Red Assay were purchased from ACD (Bio-Techne). The procedure was performed according to the manufacturer's instructions. Briefly, paraffin-embedded slides were de-paraffinized in xylene, with 2 rounds of dehydration in 100% ethanol. After air-drying, the slides were treated with H_2O_2, dipped in boiling antigen retrieval buffer, and treated with protease K for 30 min. The RNA probe was incubated for 2 hours, and RNA signaling was amplified using the amplifying reagent from ACD, followed by detection with Fast Red reagent (ACD).

IHC

Paraffin-embedded samples were cut into 4-μm sections and de-paraffinized through 3 immersions in xylene, followed by rehydration using a descending graded series of ethanol. Antigen retrieval was performed using an antigen retrieval solution (pH 6.0; Agilent), with antigens retrieved through pressing and boiling in a high-pressure cooker for 15 minutes. After antigen retrieval, sections were cooled on ice for 1 hour and washed twice with Dulbecco's PBS. Subsequently, sections were immersed in 3% H_2O_2 for 30 minutes to block endogenous peroxidase activity. After 2 additional washes with PBS, sections were incubated in a protein-blocking solution (Agilent) for 2 hours at room temperature in a humidity chamber. For mouse or rat primary antibodies, the vector M.O.M kit (Vector) was used before protein blocking. The slides were incubated with the primary antibodies overnight at 4 °C. The slides were then incubated with a horseradish peroxidase (HRP)-conjugated secondary antibody (Agilent) for 15 minutes or biotinylated anti-rat IgG (Vector) for 30 minutes, followed by incubation with ABC reagent (Vector) for 30 minutes at room temperature (RT). For the development of the HRP-labelled antibody on the sections, DAB (Agilent) was diluted and placed on the sections for the appropriate period to detect the signal. Mayer's hematoxylin (Agilent) was used to counterstain the nuclei. After counterstaining, washing and dehydration steps were performed, and the slides were covered with a mounting solution (Thermo). For immunofluorescence staining, primary antibodies were visualized using secondary antibodies conjugated to Alexa488, Cy3, or Cy5 fluorophores. The used antibodies are listed in Table 1.

Table 1. Key Resources

Reagent or resource	Source	Identifier
Antibodies		
Anti-CDX2	Abcam	Cat# ab76541 RRID: AB_1523334
Anti-CLDN4	Abcam	Cat# ab210896 RRID: AB_2732879
Anti-*H pylori*	Abcam	Cat# ab7788 RRID: AB_306077
Anti-ATP4A	MBL	Cat# DO31-3
Anti-MIST1	CST	Cat# 14896 RRID: AB_2798639
Anti-MUC5AC	Invitrogen	Cat# MA5-12178 RRID: AB_10978001
Anti-MKI67	Abcam	Cat# ab16667 RRID: AB_302459
Anti-F4/80	CST	Cat# 70076 PRID: AB_2799771
Anti-tryptase	Merck	Cat# MAB1222 RRID: AB_2206479
Anti-CD4	CST	Cat# 25229 RRID: AB_2798898
Anti-CD44v9	Cosmo Bio	Cat# LKG-M002 RRID: AB_2910608
Anti-Siglec F	BD bioscience	Cat# 552125 RRID: AB_394340
Anti-neutrophil	Abcam	Cat# ab2557 RRID: AB_303154
Anti-p-ERK1/2	CST	Cat# 4370 RRID: AB_2315112 _
Anti-p-STAT3	CST	Cat# 9134 RRID: AB_331589_
Lectin-GSII, Alexa488 conjugate	Thermo	Cat#LS21415
A488 Donkey anti-mouse IgG	Invitrogen	Cat#A21202 PRID:AB_141607
A488 Donkey anti-rabbit IgG	Invitrogen	Cat#A21206 PRID:AB_2535792
Cy3 Goat anti-Rabbit IgG	Invitrogen	Cat#A10520 PRID:AB_2534029
Cy3 Goat anti-Rat IgG	Invitrogen	Cat#A10522 PRID:AB_2534031
Cy5 Goat anti-mouse IgG	Jackson Laboratories	Cat#115-175-146 PRID:AB_2338713
Chemicals, peptides, and recombinant proteins		
SeaPlaque agarose	Lonza	Cat#50105
Fetal bovine serum	Gibco	Cat#A5256701
Penicillin/streptomycin	Thermo	Cat#15140122
Brucella broth base	Sigma	Cat#3051
Microaerobic jar	BD	Cat#260622
Gas pack	BD	Cat#260678
Mayer's haematoxylin	Agilent	Cat#S330930-2
Eosin Y	Sigma	Cat#E4009
RNA later	Invitrogen	Cat#AM7020
Serum-free protein blocks	Agilent	Cat#X0909
M.O.M reagent	Vector Laboratories	Cat#MKB-2213-1
Ready-to-Use mouse secondary antibody	Agilent	Cat#K4001
Ready-to-Use rabbit secondary antibody	Agilent	Cat#K4003
Antigen retrieval solution	Agilent	Cat#S1699
DAB substrate	Agilent	Cat#K3468
RNA later	Invitrogen	Cat#AM7020
Trizol reagent	Invitrogen	Cat#15596026
SYBR Green	Takara	Cat#RR82LR
Critical commercial assays		
ImProm-II Reverse Transcription System	Promega	Cat#A3800
RNAscope 2.5 HD Red Assay	ACD	Cat#322350
Mouse cytokine array kit	R&D Systems	Cat#ARY006
Universal genomic DNA extraction kit	TAKARA	Cat#9765

Table 1. Continued

Reagent or resource	Source	Identifier
Experimental models: Organisms/strains		
Mouse K18-hACE mice (Tg [K18-ACE2] 2 Prlmn/J)	Jackson laboratory	Cat#034860 RRID:IMSR_JAX:034860
Vero African green monkey kidney cell line	Korean cell line bank	Cat#10081
SARS-CoV-2, S type	The National Culture Collection for Pathogens	Cat#43326
Helicobacter pylori SS1	Prof. YC Lee	N/A
Software and algorithms		
gProfiler		https://biit.cs.ut.ee/gprofiler/gost
Prism		https://www.graphpad.com/scientific-software/prism/
Image J		https://fiji.sc
GSEA v4.0.3		https://www.gsea-msigdb.org/gsea/index.jsp

Immunofluorescence images were acquired using 2 different microscopy systems, an EVOS-FL fluorescence microscope, and an LSM980 confocal microscope.

Hematologic Analysis

Peripheral blood samples were obtained from the hearts of euthanized mice using a 1-mL syringe. The collected blood was transferred into 1.5-mL microtubes supplemented with 20 μL of 0.5 M ethylenediaminetetraacetic acid to prevent clotting. A comprehensive blood count was performed using a hematology analyzer (BC-5000, Mindray Global).

Cytokine Array

Mouse serum cytokine and chemokine levels were measured using a mouse cytokine array kit following the manufacturer's protocol. Mouse blood samples were centrifuged for 15 minutes at 2000 $\times$ *g*. The mean pixel intensity of each spot was quantified using ImageJ Fiji and compared with the background intensity. Thereafter, the mean intensity per duplicate was calculated and adjusted for differences in input amounts.

Transcriptomic and Bioinformatic Analyses

For the transcriptomic analysis, the same regions of the stomach were isolated using a biopsy punch and incubated in RNAlater to prevent RNA degradation. Total RNA was extracted using the TRIzol method, and RNA sequencing was conducted by Macrogen, Inc. Complete linkage and Euclidean distance, as similarity measures, were used for hierarchical clustering to analyze DEG sets. Gene enrichment, functional annotation, and pathway analyses of the significant genes were performed using gProfiler. GSEA (GSEA v4.0.3) was performed according to the manufacturer's guidelines using the expression dataset and gene set files. The predictive analysis of the immune composition of the stomach was performed using CIBERSORTx, which is an analytical tool developed by Stanford University (https://cibersortx.stanford.edu/index.php).

RNA Extraction and Reverse Transcription-quantitative Polymerase Chain Reaction

Total RNA was extracted using TRIzol reagent (Invitrogen) according to the manufacturer's protocol. cDNA was synthetised from 1 μg RNA samples using the ImProm-II reverse transcription system (Promega). Subsequent qPCR was performed with SYBR Green (Takara) using specific primers designed for the target gene. Results are presented as relative expression levels or fold changes compared with the control group. The primers used are listed in Table 2.

Table 2. Primer List for RT-qPCR

Mouse *Wfdc2* forward	TGCCTGCCTGTCGCCTCTG
Mouse *Wfdc2* reverse	TGTCCGCACAGTCCTTGTCCA
Mouse *Alpi* forward	AGGATCCATCTGTCCTTTGGT
Mouse *Alpi* reverse	TTCAGCTGCCTTCTTGTTCC
Mouse *Cldn4* forward	CGCTACTCTTGCCATTACG
Mouse *Cldn4* reverse	ACTCAGCACACCATGACTTG
Mouse *Cxcl13* forward	GGCCACGGTATTCTGGAAGC
Mouse *Cxcl13* reverse	ACCGACAACAGTTGAAATCACTC
Mouse *Dmp1* forward	AGTGAGTCATCAGAAGAAAGTCAAGC
Mouse *Dmp1* reverse	CTGTACTGGCCTCTGTCGTAGCC
Mouse *Slc7a11* forward	GACGATGGTGATGCTCTTCTC
Mouse *Slc7a11* reverse	TGGGCGTTTGTATCGAAGATA
Mouse *Cdx2* forward	AAACCTGTGCGAGTGGATG
Mouse *Cdx2* reverse	TCTGTGTACACCACCCGGTA
Mouse *Gapdh* transcript forward	AACAGCAACTCCCACTCTT
Mouse *Gapdh* transcript reverse	CCTGTTGCTGTAGCCGTATT
Mouse *Gapdh* gene forward	CCAGAACATCATCCCTGCAT
Mouse *Gapdh* gene reverse	GTAGGTCCTGCTACTGAAGCCTTA
UreB forward	CGTCCGGCAATAGCTGCCATAGT
UreB reverse	GTAGGTCCTGCTACTGAAGCCTTA

RT-qPCR, reverse transcription-quantitative polymerase chain reaction.

Bacteria Colonization Assay

To evaluate colonization with a SARS-CoV-2 infection, *H pylori* was inoculated into K18-hACE2 mice. In the experimental group, the SARS-CoV-2 challenge was performed after 4 weeks of *H pylori* infection. At 6 and 8 weeks post-*H pylori* infection, stomach specimens were obtained from the same region of K18-hACE2 mice, and total DNA was isolated using a universal genomic DNA extraction kit (Takara). For the quantitative analysis, reverse transcription-quantitative polymerase chain reaction (RT-qPCR) was performed on total stomach DNA using primers for the host-specific *Gapdh* gene and *H pylori*-specific *UreB* gene (Table 2). To estimate *H pylori* colony-forming units (CFUs) in stomach specimens, pure microbial DNA was extracted from 1×10^8 CFUs of *H pylori*, and 10-fold serially diluted DNA samples were utilized as a standard control for *UreB*. Similarly, a known amount of pure mouse genomic DNA was obtained from germ-free mice and used as a control for host *Gapdh*. Using this semi-quantitative method, we predicted the number of *H pylori* CFUs and amount of host genomic DNA in each stomach specimen. Finally, the total number of *H pylori* cells was normalized to the host genetic content acquired via RT-qPCR.

Statistical Analysis

Statistical analyses was performed using GraphPad Prism software version 9.0. Differences demonstrating statistical significance were assessed using unpaired Student *t*-test and 1-way or 2-way analysis of variance (ANOVA) with multiple comparison tests. All data and graphs were presented as the mean ± standard error of the mean (SEM). Statistical significance was set at $P < .05$.

References

1. Li G, Fan Y, Lai Y, et al. Coronavirus infections and immune responses. J Med Virol 2020;92:424–432.
2. Boechat JL, Chora I, Morais A, Delgado L. The immune response to SARS-CoV-2 and COVID-19 immunopathology - current perspectives. Pulmonology 2021; 27:423–437.
3. Jeong H, Woo Lee Y, Park IH, et al. Comparison of the pathogenesis of SARS-CoV-2 infection in K18-hACE2 mouse and Syrian golden hamster models. Dis Model Mech 2022;15:dmm049632.
4. Pandey K, Acharya A, Mohan M, et al. Animal models for SARS-CoV-2 research: a comprehensive literature review. Transbound Emerg Dis 2021;68:1868–1885.
5. Ahmad FB, Cisewski JA, Xu J, Anderson RN. COVID-19 mortality update - United States, 2022. MMWR Morb Mortal Wkly Rep 2023;72:493–496.
6. Ramos-Casals M, Brito-Zeron P, Mariette X. Systemic and organ-specific immune-related manifestations of COVID-19. Nat Rev Rheumatol 2021;17:315–332.
7. Lee NY, Lee YW, Hong SM, et al. SARS-CoV-2 Omicron variant causes brain infection with lymphoid depletion in a mouse COVID-19 model. Lab Anim Res 2023;39:8.
8. Davis HE, McCorkell L, Vogel JM, Topol EJ. Long COVID: major findings, mechanisms and recommendations. Nat Rev Microbiol 2023;21:133–146.
9. Xu E, Xie Y, Al-Aly Z. Long-term gastrointestinal outcomes of COVID-19. Nat Commun 2023;14:983.
10. Pandanaboyana S, Moir J, Leeds JS, et al; COVID PAN collaborative group. SARS-CoV-2 infection in acute pancreatitis increases disease severity and 30-day mortality: COVID PAN collaborative study. Gut 2021; 70:1061–1069.
11. Bezzio C, Saibeni S, Variola A, et al, Italian Group for the Study of Inflammatory Bowel Disease (IG-IBD). Outcomes of COVID-19 in 79 patients with IBD in Italy: an IG-IBD study. Gut 2020;69:1213–1217.
12. Pourani MR, Ganji R, Dashti T, et al; Impact of COVID-19 pandemic on patients with atopic dermatitis. Actas Dermosifiliogr 2022;113:286–293.
13. Goldenring JR, Nam KT. Oxyntic atrophy, metaplasia, and gastric cancer. Prog Mol Biol Transl Sci 2010; 96:117–131.
14. Correa P. A human model of gastric carcinogenesis. Cancer Res 1988;48:3554–3560.
15. Goldenring JR. Spasmolytic polypeptide-expressing metaplasia (SPEM) cell lineages can be an origin of gastric cancer. J Pathol 2023;260:109–111.
16. Engevik AC, Feng R, Choi E, et al. The development of spasmolytic polypeptide/TFF2-expressing metaplasia (SPEM) during gastric repair is absent in the aged stomach. Cell Mol Gastroenterol Hepatol 2016; 2:605–624.
17. Nam KT, Lee HJ, Sousa JF, et al. Mature chief cells are cryptic progenitors for metaplasia in the stomach. Gastroenterology 2010;139:2028–2037.e9.
18. Bockerstett KA, Lewis SA, Wolf KJ, et al. Single-cell transcriptional analyses of spasmolytic polypeptide-expressing metaplasia arising from acute drug injury and chronic inflammation in the stomach. Gut 2020; 69:1027–1038.
19. Jeong H, Lee B, Kim KH, et al. WFDC2 promotes spasmolytic polypeptide-expressing metaplasia through the up-regulation of IL33 in response to injury. Gastroenterology 2021;161:953–967.e15.
20. Min J, Zhang C, Bliton RJ, et al. Dysplastic stem cell plasticity functions as a driving force for neoplastic transformation of precancerous gastric mucosa. Gastroenterology 2022;163:875–890.
21. Mutoh H, Hakamata Y, Sato K, et al. Conversion of gastric mucosa to intestinal metaplasia in Cdx2-expressing transgenic mice. Biochem Biophys Res Commun 2002;294:470–479.
22. Kaparakis M, Walduck AK, Price JD, et al. Macrophages are mediators of gastritis in acute Helicobacter pylori infection in C57BL/6 mice. Infect Immun 2008; 76:2235–2239.
23. Eaton KA, Mefford M, Thevenot T. The role of T cell subsets and cytokines in the pathogenesis of Helicobacter pylori gastritis in mice. J Immunol 2001; 166:7456–7461.
24. Yamamoto J, Watanabe S, Hirose M, et al. Role of mast cells as a trigger of inflammation in Helicobacter pylori infection. J Physiol Pharmacol 1999;50:17–23.
25. Lv YP, Teng YS, Mao FY, et al. Helicobacter pylori-induced IL-33 modulates mast cell responses, benefits

bacterial growth, and contributes to gastritis. Cell Death Dis 2018;9:457.
26. Matsubara Y, Kiyohara H, Mikami Y, et al; Japan COVID-19 Task Force. Gastrointestinal symptoms in COVID-19 and disease severity: a Japanese registry-based retrospective cohort study. J Gastroenterol 2024;59:195–208.
27. Livanos AE, Jha D, Cossarini F, et al. Intestinal host response to SARS-CoV-2 infection and COVID-19 outcomes in patients with gastrointestinal symptoms. Gastroenterology 2021;160:2435–2450.e34.
28. Lee JJ, Kopetz S, Vilar E, et al. Relative abundance of SARS-CoV-2 entry genes in the enterocytes of the lower gastrointestinal tract. Genes (Basel) 2020;11:645.
29. Cheung CCL, Goh D, Lim X, et al. Residual SARS-CoV-2 viral antigens detected in GI and hepatic tissues from five recovered patients with COVID-19. Gut 2022;71:226–229.
30. Lamers MM, Beumer J, van der Vaart J, et al. SARS-CoV-2 productively infects human gut enterocytes. Science 2020;369:50–54.
31. Cardenas-Mondragon MG, Carreon-Talavera R, Camorlinga-Ponce M, et al. Epstein Barr virus and Helicobacter pylori co-infection are positively associated with severe gastritis in pediatric patients. PLoS One 2013;8:e62850.
32. Polakovicova I, Jerez S, Wichmann IA, et al. Role of microRNAs and exosomes in Helicobacter pylori and Epstein-Barr virus associated gastric cancers. Front Microbiol 2018;9:636.
33. Khanna P, Chua PJ, Bay BH, Baeg GH. The JAK/STAT signaling cascade in gastric carcinoma. Int J Oncol 2015;47:1617–1626 (Review).
34. Choi E, Hendley AM, Bailey JM, et al. Expression of activated Ras in gastric chief cells of mice leads to the full spectrum of metaplastic lineage transitions. Gastroenterology 2016;150:918–930.e13.
35. Thiem S, Eissmann MF, Elzer J, et al. Stomach-specific activation of oncogenic KRAS and STAT3-dependent inflammation cooperatively promote gastric tumorigenesis in a preclinical model. Cancer Res 2016;76:2277–2287.
36. Wang B, Zhang L, Wang Y, et al. Alterations in microbiota of patients with COVID-19: potential mechanisms and therapeutic interventions. Signal Transduct Target Ther 2022;7:143.
37. Gonzalez I, Lindner C, Schneider I, et al. Inflammation at the crossroads of Helicobacter pylori and COVID-19. Future Microbiol 2022;17:77–80.
38. Wang Y, Li Y, Zhang Y, et al. Are gastrointestinal symptoms associated with higher risk of Mortality in COVID-19 patients? A systematic review and meta-analysis. BMC Gastroenterol 2022;22:106.
39. Hayashi Y, Wagatsuma K, Nojima M, et al. The characteristics of gastrointestinal symptoms in patients with severe COVID-19: a systematic review and meta-analysis. J Gastroenterol 2021;56:409–420.
40. Sgouras D, Maragkoudakis P, Petraki K, et al. In vitro and in vivo inhibition of Helicobacter pylori by Lactobacillus casei strain Shirota. Appl Environ Microbiol 2004;70:518–526.
41. Nakajima S, Krishnan B, Ota H, et al. Mast cell involvement in gastritis with or without Helicobacter pylori infection. Gastroenterology 1997;113:746–754.
42. Kim SH, Kim J, Jang JY, et al. Mouse models of lung-specific SARS-CoV-2 infection with moderate pathological traits. Front Immunol 2022;13:1055811.
43. Eissmann MF, Dijkstra C, Jarnicki A, et al. IL-33-mediated mast cell activation promotes gastric cancer through macrophage mobilization. Nat Commun 2019;10:2735.
44. Petersen CP, Weis VG, Nam KT, et al. Macrophages promote progression of spasmolytic polypeptide-expressing metaplasia after acute loss of parietal cells. Gastroenterology 2014;146:1727–1738.e8.
45. Zhou X, Zhu H, Chen Y, et al. Role of Helicobacter pylori in gastric diseases pathogenesis cannot be ignored. Gut 2021;70:1601–1602.
46. Lee CW, Rickman B, Rogers AB, et al. Helicobacter pylori eradication prevents progression of gastric cancer in hypergastrinemic INS-GAS mice. Cancer Res 2008;68:3540–3548.
47. Davila-Collado R, Jarquin-Duran O, Dong LT, Espinoza JL. Epstein-Barr virus and Helicobacter pylori co-infection in non-malignant gastroduodenal disorders. Pathogens 2020;9:104.
48. Deng Z, Zhu J, Ma Z, et al. The mechanisms of gastric mucosal injury: focus on initial chief cell loss as a key target. Cell Death Discov 2023;9:29.
49. Meyer AR, Engevik AC, Willet SG, et al. Cystine/glutamate antiporter (xCT) is required for chief cell plasticity after gastric injury. Cell Mol Gastroenterol Hepatol 2019;8:379–405.
50. Wei Y, Lin C, Li H, et al. CXCL13 expression is prognostic and predictive for postoperative adjuvant chemotherapy benefit in patients with gastric cancer. Cancer Immunol Immunother 2018;67:261–269.
51. Liu W, Li M. The role of claudin-4 in the development of gastric cancer. Scand J Gastroenterol 2020;55:1072–1078.
52. Mutoh H, Sakurai S, Satoh K, et al. Development of gastric carcinoma from intestinal metaplasia in Cdx2-transgenic mice. Cancer Res 2004;64:7740–7747.

Received July 25, 2024. Accepted March 21, 2025.

Correspondence
Address correspondence to: Je Kyung Seong, DVM, PhD, Korea Mouse Phenotyping Center, Seoul National University, Seoul, 08826, Republic of Korea. e-mail: snumouse@snu.ac.kr; or Ki Taek Nam, DVM, PhD, Severance Biomedical Science Institute, Yonsei University College of Medicine, 50-1 Yonsei-ro, Seodaemun-gu, Seoul 03722, Korea. e-mail: kitaek@yuhs.ac; tel: 82-2-2228-0754.

CRediT Authorship Contributions

Haengdueng Jeong (Conceptualization: Lead; Data curation: Lead; Formal analysis: Lead; Investigation: Lead; Methodology: Lead; Validation: Lead; Visualization: Lead; Writing – original draft: Lead)

Sung-Hee Kim (Data curation: Equal; Formal analysis: Supporting; Investigation: Supporting; Methodology: Supporting; Supervision: Supporting)

Jiseon Kim (Data curation: Supporting; Formal analysis: Equal; Investigation: Equal; Methodology: Equal; Resources: Supporting; Visualization: Supporting)

Donghun Jeon (Data curation: Supporting; Formal analysis: Supporting; Investigation: Equal; Resources: Supporting; Visualization: Supporting)

Chanyang Uhm (Formal analysis: Supporting; Investigation: Supporting; Validation: Supporting)

Heeju Oh (Formal analysis: Supporting; Investigation: Supporting; Resources: Supporting)

Kyungrae Cho (Data curation: Supporting; Formal analysis: Supporting; Resources: Supporting)

In Ho Park (Formal analysis: Supporting; Investigation: Supporting; Resources: Supporting)
Jooyeon Oh (Formal analysis: Supporting; Investigation: Supporting; Resources: Supporting)
Jeong Jin Kim (Formal analysis: Supporting; Investigation: Supporting; Resources: Supporting)
Sang-Ho Jeong (Data curation: Equal; Resources: Equal)
Ji-Ho Park (Data curation: Equal; Resources: Equal)
Jun Won Park (Supervision: Supporting; Visualization: Supporting)
Jun-Won Yun (Project administration: Supporting; Supervision: Supporting)
Jun-Young Seo (Data curation: Supporting; Project administration: Supporting; Supervision: Supporting)
Jeon-Soo Shin (Project administration: Supporting; Supervision: Supporting)
James R. Goldenring (Writing – review & editing: Supporting)
Je Kyung Seong (Conceptualization: Equal; Funding acquisition: Equal; Project administration: Lead; Supervision: Lead; Writing – review & editing: Equal)
Ki Taek Nam, DVM, PhD (Data curation: Lead; Funding acquisition: Lead; Project administration: Lead; Supervision: Lead; Writing – review & editing: Lead)

Conflicts of interest

The authors disclose no conflicts.

Funding

This research was supported by the Bio and Medical Technology Development Program of the National Research Foundation (NRF) funded by the Korean government (MSIT) (No. RS-2021-NR057630, RS-2024-00400118, RS-2022-NR070588, RS-2023-00241446, RS-2022-NR067350) was supported by a grant (21184MFDS326) from Ministry of Food and Drug Safety in 2024.

Data Availability

All transcriptomic data have been deposited in the Korea BioData Station (K-BDS; https://www.kobic.re.kr/kona/). The readers can access the following deposited information: Bioproject Accession ID KAP240696, Sample Group Accession ID KASG156665, and Data Set ID KAD2462470. The direct accession link is as follows: https://kbds.re.kr/KAP240696. Further information and requests for resources and reagents should be directed to and fulfilled by the lead contact, Ki Taek Nam (kitaek@yuhs.ac).